



JGR Solid Earth

RESEARCH ARTICLE

10.1029/2019JB018703

Key Points:

- Novel probabilistic self-adapting fault slip inversion method is introduced
- Statistics from the ensemble of solutions allow estimating the fault slip model reliability and uncertainty
- We inspect which features of the 2016 Kumamoto earthquake source model are reliable and which are artifacts

Supporting Information:

- Supporting Information S1

Correspondence to:

M. Hallo,
miroslav.hallo@sed.ethz.ch

Citation:

Hallo, M., & Gallovič, F. (2020). Bayesian self-adapting fault slip inversion with Green's functions uncertainty and application on the 2016 $M_w7.1$ Kumamoto earthquake. *Journal of Geophysical Research: Solid Earth*, 125, e2019JB018703. <https://doi.org/10.1029/2019JB018703>

Received 12 SEP 2019

Accepted 22 FEB 2020

Accepted article online 26 FEB 2020

Bayesian Self-Adapting Fault Slip Inversion With Green's Functions Uncertainty and Application on the 2016 $M_w7.1$ Kumamoto Earthquake

M. Hallo¹ and F. Gallovič²

¹Swiss Seismological Service, ETH Zurich, Zürich, Switzerland, ²Faculty of Mathematics and Physics, Charles University, Prague, Czech Republic

Abstract Kinematic finite-extent models of earthquake sources can be determined by inverse modeling of observed waveforms and/or geodetic data. Such models are subject to significant uncertainty as a result of inaccurate observations and imperfect physical description of the complex properties of the Earth's crust. For slip inversions of large earthquakes, the major source of uncertainty is related to the uncertainty of Green's functions due to the imperfect description of the crustal model and selected parameterization of the source model. To account for both, we introduce an effective nonlinear Bayesian slip inversion with transdimensional source parameterization, including analytical representation of uncertainties of Green's functions. Our nonlinear slip inversion method relies on a self-adapting spatial parametrization of the slip distribution by means of a varying number of spline control points on the assumed fault. For the temporal parameterization, it utilizes the regularized Yoffe function with spatially varying rise time and rupture velocity. Rake angle is also treated as an unknown spatially dependent parameter. The Green's function uncertainties are included using full covariance matrices. The posterior probability density function is sampled by the transdimensional Markov chain Monte Carlo algorithm with parallel tempering. The performance of our slip inversion method is demonstrated on a synthetic test from the Source Inversion Validation project and real-data inversion of the 2016 $M_w7.1$ Kumamoto earthquake. In the latter test, we infer an ensemble of ~7,300,000 possible rupture models, representing samples of the posterior probability density, and inspect which features of these models are reliable and which are rather artifacts.

Plain Language Summary Large damaging earthquakes are caused by a rapid slip movement on large fractures in the Earth's crust. Earthshaking is then caused by a combination of released energy by the slip on the fracture (i.e., the source), propagation of generated waves through the Earth, and site-specific conditions at the place of an observer. Having observations of the earthquake from multiple locations, we can discriminate the source parameters (i.e., kinematic description of the slip) of the earthquake. We focus in this work on the inference of large earthquakes' parameters, which would take into account also the imperfect knowledge of the medium between the source and the observer. For this purpose, we utilize mathematical relations between the observed ground shaking and the description of the source to obtain a statistical description of the source model uncertainty. The spatial smoothness of source is governed by Occam's razor. Features of the earthquake source having small uncertainties are labeled as certain and vice versa. We apply this method to the destructive earthquake that happened in the Japanese prefecture Kumamoto in 2016. The interpretation supports major features as described by other researchers while pointing on some uncertain aspects of the source of this earthquake.

1. Introduction

Earthquake ground motions originate from rupture processes on faults in the Earth. Constraints on earthquake source models are essential for a better understanding of earthquake physics and for seismic hazard analysis, which is particularly significant for construction engineering and disaster mitigation planning. Kinematics of large tectonic earthquake sources can be described by finite-extent source models with heterogeneous distribution of slip on a fault and variable rupture propagation. Such source models are inferred by inverse modeling of observed seismic waveforms and/or geodetic data. The inverse solutions are generally subject to significant uncertainty (e.g., Gallovič & Ampuero, 2015; Mai et al., 2016), which should be taken into account during the evaluation of source model reliability.

1.1. Fault Slip Inversions

Approaches to the inference of fault slip models differ mainly in the chosen parameterization of the source model (e.g., Ide, 2007, and references therein). The inverse problem can be linear when a dense spatial and temporal discretization of the slip rates over the assumed fault is considered (e.g., Gallovič & Zahradník, 2010; Hartzell & Heaton, 1983; Olson & Apsel, 1982; Sekiguchi et al., 2000), as commonly used to infer kinematic sources of large crustal earthquakes (e.g., Asano et al., 2005; Asano & Iwata, 2016; Gallovič et al., 2015; Pizzi et al., 2017; Wald & Heaton, 1994). Linear inversions are typically overparameterized and hence extremely unstable, which requires regularization by, for example, the positivity of slip rates and spatial-temporal smoothing. Such regularization has to be specified a priori for the whole model, and it has been shown to be capable of producing artifacts (e.g., Zahradník & Gallovič, 2010). The issue of ill-posedness of the linear rupture inversions was tackled by exploring the eigenstructure of the inverse problem by Gallovič and Ampuero (2015). They decomposed the linear forward operator by singular value decomposition, providing a set of singular vectors in the model space. Differencing large and small singular values demonstrated that only minor part of the source model (associated with the large singular values) is correctly resolved, while the rest, lying in the operator null space, is thus basically indeterminable without additional constraints on the rupture properties and proper treatment of the associated uncertainties.

Another approach is nonlinear fault slip inversion, which relies on a spatial-temporal parameterization of the slip rate function (SRF). This particular parameterization both regularizes the solution and reduces the number of unknown parameters (e.g., Archuleta, 1984; Bouchon et al., 2002; Dettmer et al., 2014; Ji et al., 2002; Liu & Archuleta, 2004; Minson et al., 2013; Minson et al., 2014; Monelli et al., 2009; Piatanesi et al., 2007). However, these inversions require additional demands on computational power as the strongly nonlinear inverse problem should be solved by a Monte Carlo (MC) method.

In any case, each particular selection of the parameterization represents an assumption on the slip distribution and can lead to a different solution (e.g., Clévéder et al., 2004). This brings concerns about the reliability of the inferred source models due to the nonuniqueness of the inverse problem (e.g., Hartzell et al., 2007; Mai et al., 2016). In particular, Beresnev (2003) critically illustrated that the choice of a particular inversion scheme, parameterization of the SRF, spatial parameterization of the slip on the fault, and geometry of the monitoring array have a significant influence on the inferred solution. It is rather complicated to distinguish between artificial and real features of fault slip models, and hence, the importance of the consideration of the solution uncertainty rises again.

1.2. Consideration of the Uncertainties

Slip inversions with an assessment of the solution uncertainty are usually performed in the Bayesian probabilistic framework. It combines prior information on the physical model with a conditional posterior probability of model parameters given the observed data. In such a scheme, assumptions on the uncertainties of the observed data and theory need to be incorporated (e.g., Tarantola & Valette, 1982). Yagi and Fukahata (2011) and Hallo and Gallovič (2016) emphasize that the major source of such uncertainty is related to the uncertainty of Green's functions (GFs) due to the inaccuracy of the crustal model considered. The Bayesian fault slip inversions have been introduced by several recent studies. For example, Minson et al. (2013, 2014) take into account the GF variance, treating it as an unknown parameter with a uniform probability distribution. Next, Duputel et al. (2014, 2015) show the importance of considering the full covariance matrix in inversions and propose to estimate the full covariance matrices by considering a linear relationship between the GFs and random perturbations of the velocity model. Further, Hallo and Gallovič (2016) introduce so-called approximate (analytical) covariance functions inferred from observed seismograms and show that these functions can reliably represent the GF uncertainties.

Probabilistic inversions estimate the solution uncertainty for the assumed parameterization. The choice of parameterization thus has a significant influence on the inferred solution (e.g., Beresnev, 2003), and hence also on the estimated uncertainty of the solution. Therefore, it is advisable to choose the source model parameterization considering the resolution power of the observed data (e.g., Custódio & Archuleta, 2007). Overparameterization is typically associated with overfitting the observed data (i.e., noise fitting), while underparameterization is associated with oversimplified models, as also called the bias-variance trade-off problem (e.g., Bishop, 2006). This issue can be overcome by, for example,

introducing a global smoothing constraint of model parameters by using the Akaike's Bayesian information criterion (Akaike, 1980; e.g., Yabuki & Matsu'ura, 1992; Sekiguchi et al., 2000; Sekiguchi & Iwata, 2002) or by Bayesian inversion on the weight of such smoothing (e.g., Kubo, Asano et al., 2016). Another approach is to use the so-called transdimensional (trans-D) Bayesian probabilistic inversion method developed by Green (1995, 2003), where the number of model parameters is subject to inversion itself (e.g., Bodin et al., 2012; Sambridge et al., 2006). The latter approach, together with an appropriate spatially varying smoothing parameterization of the slip, allows inferring models with the data-driven spatially varying complexity. A nonlinear hierarchical Bayesian fault slip inversion with trans-D parameterization was introduced by Dettmer et al. (2014). Nevertheless, this approach does not include uncertainty of the GFs, yet it takes into account the nonstationary character of the noise in the residual waveforms (following Dettmer et al., 2007). In this paper, we introduce an effective nonlinear Bayesian slip inversion with suitable trans-D source parameterization, including analytical representation of uncertainties of GFs. The performance of our slip inversion method is demonstrated on a synthetic test from the Source Inversion Validation (SIV) project and real-data inversion of the $M_w7.1$ mainshock of the 2016 Kumamoto, Japan, earthquake sequence.

2. Method

Here we introduce our nonlinear Bayesian fault slip inversion method with trans-D parameterization of the SRFs on the fault and with implemented uncertainty of GFs.

2.1. Finite-Extent Source Representation

The displacement wavefield $\mathbf{u}(\xi, t)$ measured at receiver position ξ and time t is related to the SRF $\Delta\dot{u}(\xi, t)$ distributed along the fault by the representation theorem (e.g., Aki & Richards, 2002). Assuming that the shear slip direction does not change in time, the representation theorem reads

$$\mathbf{u}(\xi, t) = \iint_{\Sigma} \Delta\dot{u}(\xi, t)^* \mathbf{G}(\xi, t; \xi) d\Sigma(\xi), \quad (1)$$

where $*$ denotes temporal convolution and \mathbf{G} represents the displacement waveform at observation point ξ corresponding to a slip rate pulse at position ξ on the fault Σ (here called as GF).

The fault geometry is expected to be fixed and given a priori (e.g., from geological mapping, from aftershock distribution, or as a result of a centroid moment tensor inversion). The fault plane is spatially discretized into N_{Σ} uniform rectangular subfaults of area $\Delta\Sigma$. These subfaults are assumed to be small with respect to the used wavelengths and source-receiver distances to be considered as point sources. The subfaults are characterized by their strike and dip angles, while rake angles ϑ_i (i.e., slip direction on the subfault i) are subject to the inversion. Therefore, we express the GF for an arbitrary rake angle as a linear combination of two GFs ($\hat{\mathbf{G}}$ and $\tilde{\mathbf{G}}$) for two perpendicular rake angles $\hat{\vartheta}$ and $\tilde{\vartheta}$ given a priori. Then, the formula for the n th displacement component reads

$$u_n(\xi, t) = \Delta\Sigma \sum_{i=1}^{N_{\Sigma}} \Delta\dot{u}_i(t)^* \left(\hat{G}_{ni}(\xi, t) \cos(\vartheta_i - \hat{\vartheta}) + \tilde{G}_{ni}(\xi, t) \cos(\tilde{\vartheta} - \vartheta_i) \right), \quad (2)$$

where $\hat{G}_{ni}(\xi, t)$ and $\tilde{G}_{ni}(\xi, t)$ are n th components of the two GFs for subfault i and $\Delta\dot{u}_i(t)$ is the respective SRF. The advantage of such formulation is the possibility to precompute GFs for all receivers and subfaults prior to the inversion for arbitrarily rake angles on the given fault. We use the discrete wavenumber method (Bouchon, 1981) for computing GFs in this work, but our method is not restricted to this particular choice (i.e., other approaches for numerical or empirical determination GFs could be used as well).

2.2. Rupture Parameterization

In our approach, we utilize a spatial-temporal parametrization of SRF, $\Delta\dot{u}_i(t)$, and treat the problem as nonlinear. The time dependence of SRF is modeled by regularized Yoffe function Y introduced by Tinti et al. (2005), reading

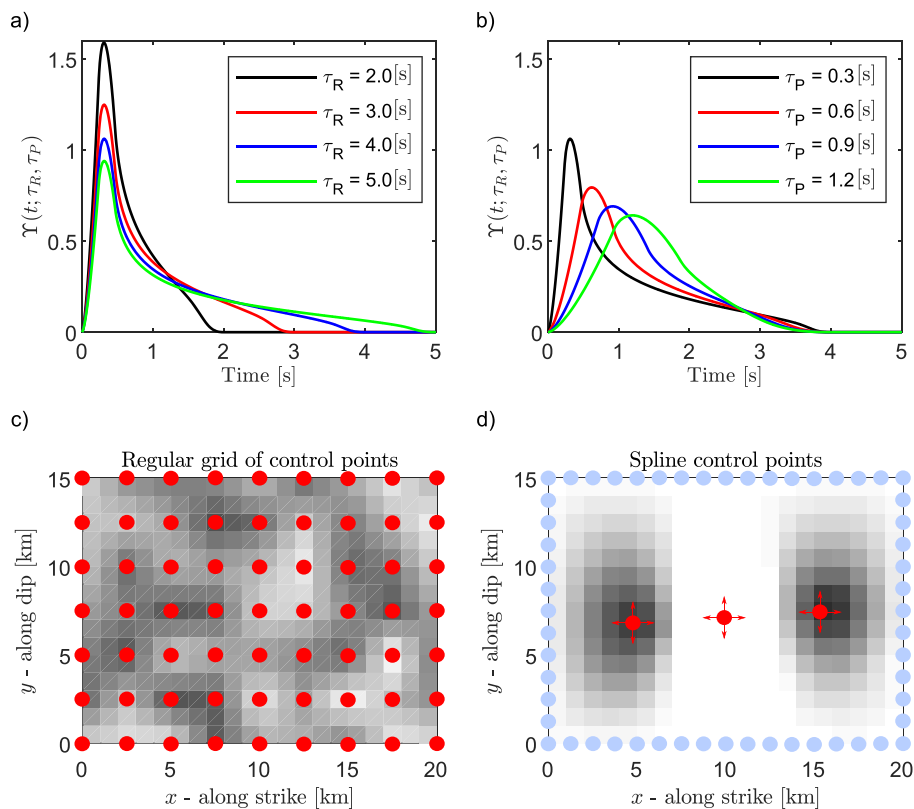


Figure 1. Spatial-temporal parametrization of the SRF. (top) Examples of various (temporal) regularized Yoffe functions for (a) fixed peak time $\tau_P = 0.3$ s and (b) fixed rise time $\tau_R = 4.0$ s. For the variable parameter, see legend. (bottom) Schemes of two systems of control points used for the spatial parameterization. Shaded gray rectangles represent subfaults discretizing the fault for the evaluation of the representation integral. Positions of the control points on the fault are shown by red circles for (c) the regular grid and (d) the system of spline points (see text). Blue circles show (optional) auxiliary control points setting slip to zero on the fault edges.

$$\Delta \dot{u}_i(t) = A_i Y(t - t_i^0; \tau_i^R, \tau_i^P), \quad (3)$$

where t_i^0 is rupture time, A_i is slip, τ_i^R is rise time (duration of slip), and τ_i^P is so-called peak time (duration of initial positive slip acceleration), all respective to subfault i . The regularized Yoffe function (see examples in Figures 1a and 1b) is a nonnegative function of a unit area, it can be expressed analytically, and it is compatible with rupture dynamics (Bizzarri, 2012). Therefore, it is suitable as a shape of SRF for fast forward problem computations.

The initiation of the rupture process at the subfaults is defined by rupture times t_i^0 (see equation (3)). We assume that the rupture propagates from hypocenter \mathbf{h} (three-component vector specifying its position on the fault surface and the origin time). The rupture propagates with rupture-front velocity $v^0(\xi)$, which is a function of position on the fault plane. The rupture times are then formally a solution of the two-dimensional eikonal equation, describing the propagation of the rupture front along the fault. The eikonal equation can be numerically solved on a dense grid by a method relying on a systematic application of the Huygens' principle in the finite-difference approximation (Podvin & Lecomte, 1991). Nevertheless, any other rupture-front propagation solver can be used as well. We treat hypocenter \mathbf{h} and rupture-front velocity function $v^0(\xi)$ as model parameters instead of the rupture times t_i^0 themselves. It forbids nucleation of the rupture from multiple spatially separated areas and enforces causality.

Parameters ϑ_i , A_i , τ_i^R , and τ_i^P are assigned to positions of the subfaults' centers on the fault. In our approach, these parameters are interpolated from a sparse grid of so-called control points. We define two different interpolation methods with a different system of the control points. In the first method, we use a fixed

regular grid of control points distributed over the whole fault (Figure 1c). Each “regular” control point c has assigned values of the rake angle, rupture-front velocity, rise time, and peak time (i.e., ϑ_c , v_c^0 , τ_c^R , and τ_c^P , respectively). The value of a parameter at the i th subfault position is obtained by bilinear interpolation from the regularly distributed control points with assigned values stored in matrix Γ . In the case of rupture-front velocity $v^0(\xi)$, the values in the control points are interpolated by the bilinear interpolation into a dense finite-difference grid used by the rupture-front propagation solver, and then the resulting rupture times are resampled to the subfault positions for the representation integral calculation.

For the spatial parametrization of slip A_i we use a different system of control points as it is the leading parameter. Following the idea of Causse et al. (2017), we utilize a self-adapting parametrization with varying number of control points where the density of the control points can vary spatially. Such parameterization can effectively adapt to the heterogeneity of slip such as to the case of a multiple asperity source model. The used system of control points consists of a variable number of points N_Φ (called as “spline points”) arbitrarily distributed over the fault plane (see Figure 1d). These spline points are allowed to move over the whole fault surface during the inversion. Each “spline” control point c is assigned by a value of slip and position on the fault (i.e., A_c , x_c , and y_c). Slip A_i at the i th subfault position is evaluated using biharmonic spline interpolation (Sandwell, 1987; see Appendix A). As an optional feature, the interpolation is performed with enforced zero slip at the fault edges; this is achieved by adding fixed auxiliary spline points regularly distributed at the fault edges with assigned zero slip (see Figure 1d). The slip on the fault is then parameterized by assigned properties of all “spline” control points stored in matrix Φ of size $(N_\Phi \times 3)$.

We note that other approaches can be used for the self-adapting spatial parametrization of slip. Nevertheless, it is advisable to use parameterization suitable for continuous and smooth functions (e.g., Hawkins et al., 2019). For example, Voronoi cells considered by Dettmer et al. (2014) introduce non-smooth sharp boundaries between two neighboring cells, which may cause unexpected artifacts in this case. A suitable alternative may be parameterization by the tree structures (Hawkins & Sambridge, 2015), which would also lead to the desirable smooth spatially varying complexity of slip on the fault. Nevertheless, one of the advantages of our parameterization by spline points allows representing the smooth slip distribution on a simple circular (dynamic-like) crack by just one control point, while allowing increasing the physically significant complexity of slip by increasing the number of spline points. Hence, our parameterization can be considered as physically oriented, while the tree structures would be resolvability oriented.

2.3. Forward Problem

The representation theorem in equation (2) shows straightforward relation among the synthetic displacement, GFs, and SRF on the assumed fault. For the sake of the numerical computations, the expression in equation (2) is rewritten in the form of discrete-time samples as

$$u_n^r = \Delta \Sigma \Delta t \sum_{i=1}^{N_\Sigma} \sum_{s=1}^{N_T} \Delta \hat{u}_i^s \left(\hat{G}_{ni}^{r-s} \cos(\vartheta_i - \hat{\vartheta}) + \tilde{G}_{ni}^{r-s} \cos(\tilde{\vartheta} - \vartheta_i) \right), \quad (4)$$

where Δt is the temporal sampling interval of SRF with N_T samples in total. Indexes r and s denote temporal samples of the waveforms and SRFs, respectively. The GFs, \hat{G}_{ni} and \tilde{G}_{ni} , for two perpendicular rakes ($\hat{\vartheta}$ and $\tilde{\vartheta}$) are precomputed before the inversion for all receivers and components n , and subfaults i . Then, the n th synthetic component can be directly computed for a given set of SRFs $\Delta \hat{u}_i$ and respective rake angles ϑ_i using matrix multiplication.

In the inverse problem, the forward problem of equation (4) needs to be solved many times for various sets of trial model parameters (i.e., models), defined in our parameterization (see section 2.2) as vector

$$\mathbf{w}_{N_\Phi} = (\mathbf{h}, \text{vec}(\boldsymbol{\Gamma}), \text{vec}(\boldsymbol{\Phi})), \quad (5)$$

where $\text{vec}(\cdot)$ denote vectorization of a matrix. Vectors \mathbf{h} and $\text{vec}(\boldsymbol{\Gamma})$ have a fixed size, while $\text{vec}(\boldsymbol{\Phi})$ have length of $N_\Phi \times 3$. Such model vector \mathbf{w}_{N_Φ} fully parameterizes the spatial-temporal rupture propagation on the fault for a particular number of spline points N_Φ . The forward problem, where synthetic waveforms on all receivers for a given model \mathbf{w}_{N_Φ} are predicted by equation (4), can be expressed using a forward operator $g(\cdot)$ as

$$\mathbf{d} = g(\mathbf{w}_{N_\Phi}), \quad (6)$$

where vector \mathbf{d} contains all synthetic waveforms predicted on all three-component receivers.

To summarize, the forward computation consists of the following steps:

1. Interpolate rake, rise time, and peak time parameters from the regular fixed grid stored in matrix Γ into all subfaults.
2. Interpolate rupture-front velocity from the regular grid stored in matrix Γ into the dense finite-difference grid of the eikonal solver. Evaluate rupture times assuming rupture-front propagation from the hypocenter \mathbf{h} . Resample the rupture times to all subfaults.
3. Perform biharmonic spline interpolation of slip from the given number of spline points N_Φ stored in matrix Φ to all the subfaults.
4. Evaluate SRFs for all the subfaults using equation (3).
5. Perform the discrete temporal convolution of SRFs and GFs and summation over subfaults following equation (4).

2.4. Trans-D Bayesian Inference

Following Tarantola and Valette (1982) and Tarantola (2005), we introduce an abstract n -dimensional vector space \mathcal{R}^n , where each vector represents a model of the system. Such multidimensional space is called model space, and each model is denoted by vector \mathbf{w} , where $\mathbf{w} \in \mathcal{R}^n$. In analogy, the observed data are treated as data vector \mathbf{d}_{obs} in an abstract multidimensional linear data space of dimension given by the total number of measured data. As we assume a varying number of spline points N_Φ , the length of the model vector \mathbf{w} and consequently the dimension n of its model space vary. This leads to trans-D formulation, where the number of dimensions of the model space is treated as an unknown parameter (e.g., Fan & Sisson, 2011; Green, 1995, 2003; Sambridge et al., 2006).

Let us assume that we have a countable collection of model states \mathcal{K} indexed by parameter $k \in \mathcal{K}$. Each model state has respective n_k -dimensional model vector \mathbf{w}_k in its own model space, $\mathbf{w}_k \in \mathcal{R}^{n_k}$. The union state space \mathcal{X} for across-model simulations is defined following Green (2003) as

$$\mathcal{X} = \bigcup_{k \in \mathcal{K}} (\{k\} \times \mathcal{R}^{n_k}). \quad (7)$$

Then, we aim to explore trans-D models $\mathbf{m} = (k, \mathbf{w}_k)$ as an element of the union state space \mathcal{X} ($\mathbf{m} \in \mathcal{X}$), which can be achieved by a specific MC sampler, as explained in section 2.5.

The physical measurements \mathbf{d}_{obs} and models \mathbf{m} are subject to uncertainties. In the Bayesian framework (e.g., Tarantola, 2005), these uncertainties are represented by multidimensional probability density functions (PDFs). The Bayesian solution of an inverse problem is then given by the posterior (conditional) PDF on model parameters,

$$p(\mathbf{m} | \mathbf{d}_{obs}) = \frac{p(\mathbf{m}) p(\mathbf{d}_{obs} | \mathbf{m})}{\int p(\mathbf{m}) p(\mathbf{d}_{obs} | \mathbf{m}) d\mathbf{m}}, \quad (8)$$

where $p(\mathbf{m})$ is a prior PDF on model parameters and $p(\mathbf{d}_{obs} | \mathbf{m})$ is a conditional PDF of data given model \mathbf{m} , that is, so-called likelihood function. Equation (8) can be rewritten for the case of trans-D models $\mathbf{m} = (k, \mathbf{w}_k)$ following Green (2003) as

$$p(\mathbf{m} | \mathbf{d}_{obs}) = p(k, \mathbf{w}_k | \mathbf{d}_{obs}) = \frac{p(k) p(\mathbf{w}_k | k) p(\mathbf{d}_{obs} | k, \mathbf{w}_k)}{\sum_{k' \in \mathcal{K}} \int_{\mathcal{R}^{n_{k'}}} p(k') p(\mathbf{w}'_{k'} | k') p(\mathbf{d}_{obs} | k', \mathbf{w}'_{k'}) d\mathbf{w}'_{k'}}, \quad (9)$$

where $p(k)$ is a prior probability on model states (number of spline points), $p(\mathbf{w}_k | k)$ is a prior PDF on model parameters given state k , and $p(\mathbf{d}_{obs} | k, \mathbf{w}_k) = p(\mathbf{d}_{obs} | \mathbf{m})$ is the likelihood function given trans-D model \mathbf{m} .

The likelihood function $p(\mathbf{d}_{obs} | \mathbf{m})$ evaluates how well the given model \mathbf{m} describes the observed waveforms \mathbf{d}_{obs} by means of a misfit with synthetic waveforms \mathbf{d} predicted by equation (4). It can be expressed for assumed Gaussian data errors (e.g., Tarantola, 2005) as

$$p(\mathbf{d}_{obs}|\mathbf{m}) = \text{const.} \exp\left(-\frac{1}{2}\mathcal{L}(\mathbf{m})\right), \quad (10)$$

with the misfit function $\mathcal{L}(\mathbf{m})$ expressed in matrix form as

$$\mathcal{L}(\mathbf{m}) = (\mathbf{d}_{obs} - g(\mathbf{m}))^T \mathbf{C}_D^{-1} (\mathbf{d}_{obs} - g(\mathbf{m})). \quad (11)$$

The Gaussian covariance matrix \mathbf{C}_D characterizes cross-covariances of misfits, which can encompass expected errors of both observed data and theory (Duputel et al., 2014). The expected errors of the measured data and theory (i.e., uncertainties of GFs) are treated as invariant during exploration of the model space in our approach, which is in accord with their formal definition. The covariance matrix \mathbf{C}_D can be decomposed by Cholesky decomposition as

$$\mathbf{C}_D^{-1} = \mathbf{W}^T \mathbf{W}, \quad (12)$$

where \mathbf{W} is an upper triangular matrix. Substituting equation (12) into equation (11), the misfit function reads

$$\mathcal{L}(\mathbf{m}) = (\mathbf{Wd}_{obs} - \mathbf{Wg}(\mathbf{m}))^T (\mathbf{Wd}_{obs} - \mathbf{Wg}(\mathbf{m})), \quad (13)$$

where \mathbf{Wd}_{obs} and $\mathbf{Wg}(\mathbf{m})$ are so-called standardized observed and synthetic waveforms, respectively (Hallo & Gallovič, 2016). Note that equations (10)–(13) are valid independently on the number of dimensions of the model vector \mathbf{m} , which influences implicitly only the forward computation by $g(\cdot)$. This means that model vectors from different subspaces of \mathcal{X} (i.e., $\mathbf{w}_k \in \mathcal{X}$ and $\mathbf{w}'_{k'} \in \mathcal{X}$, where $k \neq k'$) that reproduce identical synthetic waveforms result in equal misfit to the observed data. This feature is essential for the trans-D model balance (see section 2.5).

Concerning the covariance matrix \mathbf{C}_D , we assume it is dominated by modeling errors of the GFs due to the inaccuracy of the Earth crust model considered (e.g., Yagi & Fukahata, 2011). Ambient noise and instrumental artifacts are typically negligible when dealing with large events or can be avoided by station exclusion. We include the modeling errors in covariance matrix \mathbf{C}_D following the approach by Hallo and Gallovič (2016). They compose \mathbf{C}_D from discrete-time samples of approximate covariance functions (ACF or SACF; see Appendix B). These approximate covariance functions are based on consideration of possible influence of the randomly perturbed (assumed inaccurate) velocity model on the GFs. In this work, we particularly assume nonstationary ACFs for velocity model uncertainty 15% (for details, see Hallo & Gallovič, 2016). In the multistation and multicomponent inversions, data covariance matrix \mathbf{C}_D has a block-diagonal structure. The covariance matrices for each waveform are arranged along the diagonal, while the off-diagonal blocks are intercomponent and interstation cross-covariance (not assumed in the present application, i.e., are set to zero). Finally, a station-specific water level is added to the diagonal to stabilize the Cholesky decomposition of the block-structured covariance matrix. As the water level, 25% of the maximum variance from all three station components was used.

2.5. Sampling of the Trans-D Posterior PDF

To draw random samples from the trans-D posterior PDF in equation (9), we utilize the reversible-jump Markov chain Monte Carlo (MCMC) algorithm by Green (1995, 2003). It is based on the Metropolis-Hastings algorithm (Hastings, 1970; Metropolis et al., 1953), which samples the posterior PDF by a series of random steps in the model space. The used algorithm extends the Metropolis-Hastings algorithm to cases when the model changes the state (i.e., makes trans-D steps) within the Markov chain steps. By such MCMC approach, model $\mathbf{m} = (k, \mathbf{w}_k)$ is perturbed in each MC step by creating a new (proposed) model $\mathbf{m}' = (k', \mathbf{w}'_{k'})$ with a forward step probability drawn from proposal distribution $q(\mathbf{m}'|\mathbf{m})$ within the whole state space \mathcal{X} . The proposed model \mathbf{m}' is then accepted or rejected based on the acceptance probability (Metropolis et al., 1953). Following Green (2003), the acceptance probability $\alpha(\mathbf{m} \rightarrow \mathbf{m}')$ in a general form reads

$$\alpha(\mathbf{m} \rightarrow \mathbf{m}') = \min\left(1, \frac{p(k')}{p(k)} \frac{p(\mathbf{w}'_{k'}|k')}{p(\mathbf{w}_k|k)} \frac{p(\mathbf{d}_{obs}|\mathbf{m}')}{p(\mathbf{d}_{obs}|\mathbf{m})} \frac{q(\mathbf{m}|\mathbf{m}')}{q(\mathbf{m}'|\mathbf{m})} |\mathbf{J}| \right), \quad (14)$$

where $q(\mathbf{m}|\mathbf{m}')$ is the proposal distribution of the reverse step ($\mathbf{m}' \rightarrow \mathbf{m}$) across \mathcal{X} , $p(k')$ is a prior probability on the proposed model state k' , $p(\mathbf{w}'_{k'}|k')$ is prior PDF on model parameters under the proposed state k' , and $p(\mathbf{d}_{obs}|\mathbf{m}')$ is the likelihood function of the proposed model \mathbf{m}' . The Jacobian \mathbf{J} is to account for the space volume change in the transformation $\mathbf{m} \rightarrow \mathbf{m}'$, and it can be omitted (it is unity) for the problem considered in this research (see Bodin & Sambridge, 2009; Sambridge et al., 2006). Equation (14) resembles the standard Metropolis-Hastings acceptance probability (Hastings, 1970) and includes it as a special case when $\dim(\{k\}) = 1$. The abstract meaning of the proposal distribution q from Equation (14) is overcome in the reversible-jump algorithm by proposing that trans-D moves through dimension matching (see Dettmer et al., 2010; Gallagher et al., 2009; Green, 1995, 2003; Sambridge et al., 2006).

In our particular case, each model state consists of a different number of spline points; that is, index k has the meaning of the number of spline points N_Φ , that is, $(k, \mathbf{w}_k) \equiv (N_\Phi, \mathbf{w}_{N_\Phi})$, where $k = 1, 2, 3, \dots, k_{max}$. The difference in the number of dimensions of two adjacent model spaces \mathcal{R}^{n_k} and $\mathcal{R}^{n_{k+1}}$ is in our case $(n_{k+1} - n_k) = 3$, as we define every spline point by three parameters (see section 2.2). Further, the model state transitions are considered in one Markov chain step only between neighboring model states. It can be a model state with either one extra or one less spline point. This is so-called birth-death MCMC (e.g., Geyer & Moller, 1994), and it consists of three move types that occur with probabilities j_P , j_B , and j_D , such that

$$1 = j_P + j_B + j_D, \quad (15)$$

where j_P is the probability of a “perturb” move with no change in dimension ($k' = k$), j_B is the probability of “birth” of new dimensions (i.e., creation of one arbitrarily spline point, $k' = k+1$), and j_D is the probability of “death”, meaning reducing dimensions (i.e., deleting one arbitrarily spline point, $k' = k - 1$). The probabilities of birth and death moves are equal, so as not to prefer either birth or death proposals. The probability of the perturb move may be higher to let the MCMC sampler explore various parameter combinations of the model with temporarily fixed model state k . The choice of these probabilities is arbitrary (as far as $j_B = j_D$), as it only influences the efficiency of the sampling algorithm and does not alter the posterior PDF itself (see Dettmer et al., 2010; Green, 1995). We set these probabilities as $j_P = 0.9$ and $j_B = j_D = 0.05$; nevertheless, they can be adjusted according to the particular inversion.

Concerning the propositions of perturbations of the existing model parameters, we utilize Gaussian proposal distribution, which is recentered after each step to the present value. Then, in the case of the perturb move, the trans-D MCMC behaves like a Gaussian random-walk MCMC. In such process, the forward and reverse steps are reversible, that is, $q(\mathbf{m}'|\mathbf{m}) = q(\mathbf{m}|\mathbf{m}')$. The acceptance probability $\alpha_P(\mathbf{m} \rightarrow \mathbf{m}')$ for this scenario of no change of state can be obtained from equation (14) as

$$\alpha_P(\mathbf{m} \rightarrow \mathbf{m}') = \min\left(1, \frac{p(\mathbf{w}'_k|k)}{p(\mathbf{w}_k|k)} \frac{p(\mathbf{d}_{obs}|\mathbf{m}')}{p(\mathbf{d}_{obs}|\mathbf{m})} \right). \quad (16)$$

The acceptance probabilities for the birth and death moves $\alpha_B(\mathbf{m} \rightarrow \mathbf{m}')$ and $\alpha_D(\mathbf{m} \rightarrow \mathbf{m}')$ are given in analogy to Sambridge et al. (2006) as

$$\alpha_B(\mathbf{m} \rightarrow \mathbf{m}') = \min\left(1, \frac{p(k+1)}{p(k)} \frac{p(\mathbf{w}'_{k+1}|k+1)}{p(\mathbf{w}_k|k)} \frac{p(\mathbf{d}_{obs}|\mathbf{m}')}{p(\mathbf{d}_{obs}|\mathbf{m})} \frac{q_{k+1}^D}{q_k^B} \right), \quad (17)$$

$$\alpha_D(\mathbf{m} \rightarrow \mathbf{m}') = \min\left(1, \frac{p(k-1)}{p(k)} \frac{p(\mathbf{w}'_{k-1}|k-1)}{p(\mathbf{w}_k|k)} \frac{p(\mathbf{d}_{obs}|\mathbf{m}')}{p(\mathbf{d}_{obs}|\mathbf{m})} \frac{q_k^B}{q_{k-1}^D} \right). \quad (18)$$

Here q_k^B and q_k^D are probability densities of birth or death of one spline point, respectively, which can be expressed similarly to those in Bodin et al. (2012). In particular, we evaluate the probability density of birth (spontaneous occurrence) of a new spline point on a random location on the fault of finite-size $x_\Sigma \times y_\Sigma$ (independent of k) and the probability of death (removal) of one arbitrary spline point from all present (k) or all proposed ($k+1$).

Further, the prior PDFs in equations (16)–(18) can be simplified assuming efficiently homogenous prior PDF (i.e., a weakly informative proper prior; see Appendix C) on model parameters under the same state, that is, $p(\mathbf{w}'_k|k) = p(\mathbf{w}_k|k)$. Then, the prior PDF on model parameters under the state $k+1$, that is, $p(\mathbf{w}'_{k+1}|k+1)$ is the prior PDF at state k , that is, $p(\mathbf{w}_k|k)$, augmented by the prior of a random occurrence of one spline point on the fault of size $x_\Sigma \times y_\Sigma$. Consequently, proposal distributions are in balance with prior PDFs on model parameters, that is, $\frac{p(\mathbf{w}'_{k+1}|k+1)}{p(\mathbf{w}_k|k)} \cdot \frac{q_k^P}{q_{k+1}^B} = 1$ and $\frac{p(\mathbf{w}'_{k-1}|k-1)}{p(\mathbf{w}_k|k)} \cdot \frac{q_{k-1}^B}{q_k^P} = 1$ (see supporting information Text S1).

Finally, for the prior probability on the model states we prescribe a reciprocal distribution, $p(k) \propto k^{-1}$, working as Occam's razor (see supporting information Figure S1a). Such distribution would result in improper probability in \mathbb{R} ; however, it is proper (i.e., normalizable to 1) in our case of a countable collection of model states $k \in \mathcal{K}$. As a result, the birth move is penalized with increasing number of spline points, while the death move acceptance probability increases with the number of spline points (see equations (20) and (21)). Hence, a better value of misfit between data and synthetics is required to increase the number of spline points (and thus potentially the slip complexity) in the MCMC algorithm. We want to emphasize that the number of spline points in the posterior trans-D models is governed by the data misfit and the prior probability on the model states only. Hence, the number of spline points is independent of a particular slip distribution as far as it reproduces the same data misfit.

To increase the efficiency of the trans-D MCMC sampler, we apply the parallel tempering (PT) method introduced by Sambridge (2014). The PT sampling algorithm is similar to the simulated annealing method (Kirkpatrick et al., 1983), modifying the posterior PDF by an additional parameter called temperature $\gamma \geq 1$. The random samples are then drawn following such modified posterior PDF assuming multiple values of temperature γ (multiple parallel trans-D Markov chains), while at least one chain has $\gamma = 1$ (see also Valentová et al., 2017; Gallovič et al., 2019a & Gallovič et al., 2019b). The acceptance probabilities for perturb, birth, and death moves in equations (16)–(18) with canceled homogenous prior PDFs are then modified as follows:

$$\alpha_P(\mathbf{m} \rightarrow \mathbf{m}', \gamma) = \min\left(1, \left(\frac{p(\mathbf{d}_{obs}|\mathbf{m}')}{p(\mathbf{d}_{obs}|\mathbf{m})}\right)^{1/\gamma}\right), \quad (19)$$

$$\alpha_B(\mathbf{m} \rightarrow \mathbf{m}', \gamma) = \min\left(1, \frac{k}{k+1} \left(\frac{p(\mathbf{d}_{obs}|\mathbf{m}')}{p(\mathbf{d}_{obs}|\mathbf{m})}\right)^{1/\gamma}\right), \quad (20)$$

$$\alpha_D(\mathbf{m} \rightarrow \mathbf{m}', \gamma) = \min\left(1, \frac{k}{k-1} \left(\frac{p(\mathbf{d}_{obs}|\mathbf{m}')}{p(\mathbf{d}_{obs}|\mathbf{m})}\right)^{1/\gamma}\right). \quad (21)$$

Arbitrary trans-D chains are allowed to exchange the temperatures with a probability given by a balance condition for the swap (e.g., Sambridge, 2014). Finally, the ensemble of solutions following the posterior PDF is formed only by random samples at temperature $\gamma = 1$, which sample the original posterior PDF.

To summarize, the utilized trans-D MCMC algorithm with PT at each Markov chain step is as follows:

1. randomly selects the move type (perturb/birth spline/spline death);
2. randomly perturbs the current model to create a new (proposed) model;
3. creates a new spline point or deletes an existing spline point (birth or death moves only);
4. computes the forward problem and then accepts or rejects the proposed model based on the respective acceptance probability; and
5. tries to exchange the temperature γ with another Markov chain.

3. Computational Workflow

We have developed Fortran90 code PSI (Parametric Slip Inversion), for application of the methodology as described in section 2. The code includes the eikonal finite-difference solver written in C (Podvin & Lecomte, 1991), PT Fortran90 interface by Sambridge (2014), Fortran90 subroutine for computing covariance matrices from ACF by Hallo and Gallovič (2016), and some Fortran90 subroutines from linear multitime-window earthquake slip inversion (LinSlipInv) by Gallovič et al. (2015). Inputs of PSI are

filtered observed waveforms, precomputed GFs by an arbitrary method in a fixed format, and settings of the inversion. The output of PSI is an ensemble of models drawn from the posterior trans-D PDF and log files with the sampling progress record. PSI is parallelized using the Message Passing Interface (MPI), and it can be run on supercomputing clusters as well as on personal computers. For the maximum performance, each CPU core is assigned to a single MPI process (MPI node). In the case of multiple-CPU run, one CPU core hosts the “master” process that controls the exchanges of temperatures among “slave” processes, which run on all other CPU cores and perform all the calculations. The PSI code workflow (see Figure 2) is as follows.

First, PSI dynamically allocates the random-access memory (RAM) on all deployed computational nodes and read the input data. It prepares the data covariance matrix \mathbf{C}_D (blue star in Figure 2), utilizing the method of the user’s choice (ACF, SACF, or diagonal station-constant matrix). Then, it computes standardized observed waveforms \mathbf{Wd}_{obs} and standardized GFs for two perpendicular rakes $\mathbf{W} \cdot \text{vec}(\tilde{\mathbf{G}}_i)$ and $\mathbf{W} \cdot \text{vec}(\mathbf{G}_i)$ (cyan star in Figure 2; see equation (12)). This step has a significant impact on the efficiency of the code as the inverse of the covariance matrix and the standardized waveforms do not need to be recomputed at each Markov chain step. At the same time, we can delete the large covariance matrix and free some RAM. The standardized waveforms are then saved to the hard drive to skip this RAM-demanding step in case of multiple-CPU run (see the first conditional operation in Figure 2).

Next, PSI creates initial source models (magenta star in Figure 2) for all “exploration” ($\gamma > 1$) and “sampling” ($\gamma = 1$) Markov chains of the PT algorithm, independently on each of the deployed CPU. These initial source models have assigned random model parameters b (i.e., $b = w_k^l$) drawn from uniform or Gaussian PDFs. The distribution of the initial random models may be arbitrary (as far as it contains randomness), as it only influences the efficiency of the sampling algorithm in terms of the necessary length of the subsequent “burn-in” phase. Nevertheless, every initial parameter has to satisfy all constraints, in particular, to lie within an interval of prescribed (physically plausible) values, that is, $B = [b_{\min}, b_{\max}]$. If any of the initial parameters exceed their limits, then a new initial random model is generated. The ranges are preferably set broad (input by the user) to view the prior PDF as efficiently homogeneous (Appendix C), that is,

$$p(b) = \begin{cases} \frac{1}{b_{\max} - b_{\min}} & \text{if } b \in B, \\ 0 & \text{otherwise.} \end{cases} \quad (22)$$

This is so not to prefer any particular value between b_{\min} and b_{\max} during the model space exploration by the random walk (i.e., weakly informative proper prior). Note that the slip distribution is initiated by a single spline point ($N_\Phi = 1$) randomly generated on the fault surface. It ensures a simple, yet random, initial distribution of the slip.

As a next step, PSI initiates the burn-in phase of PT (Sambridge, 2014) on all the deployed CPUs. In this phase, various trans-D models are explored by the Markov chains, but the model samples are excluded from the ensemble of solutions (i.e., no model is saved). PSI performs testing of trial source models (forward problem in equation (4); green star in Figure 2) against the observed data and accepts/rejects them based on the Metropolis-Hastings acceptance probabilities (equations (19)–(21); lime star in Figure 2). The perturbed trial models (orange star in Figure 2) are proposed by a Gaussian random walk in the model space. The utilized random walk algorithm (see Appendix C for details) ensures efficiently homogeneous prior PDFs (equation (22)) within the whole range of parameter-specific interval $B = [b_{\min}, b_{\max}]$ (see examples in the supporting information Figures S1b and S1c). However, reaching boundaries b_{\min} and b_{\max} is considered as undesirable. Such a situation appears if limits of the interval B are set as too tight or if there is too low information content in the data (data contamination by strong uncorrelated white noise, uneven station distribution, limited frequency range, etc.). Hence, these incidents are monitored and continuously recorded in log files. We point out that this burn-in phase is necessary because the set of initial models does not follow the posterior PDF explicitly. The length of this phase differs for each setting, and it could be estimated by inspecting the data variance reduction, being continuously recorded in the log files.

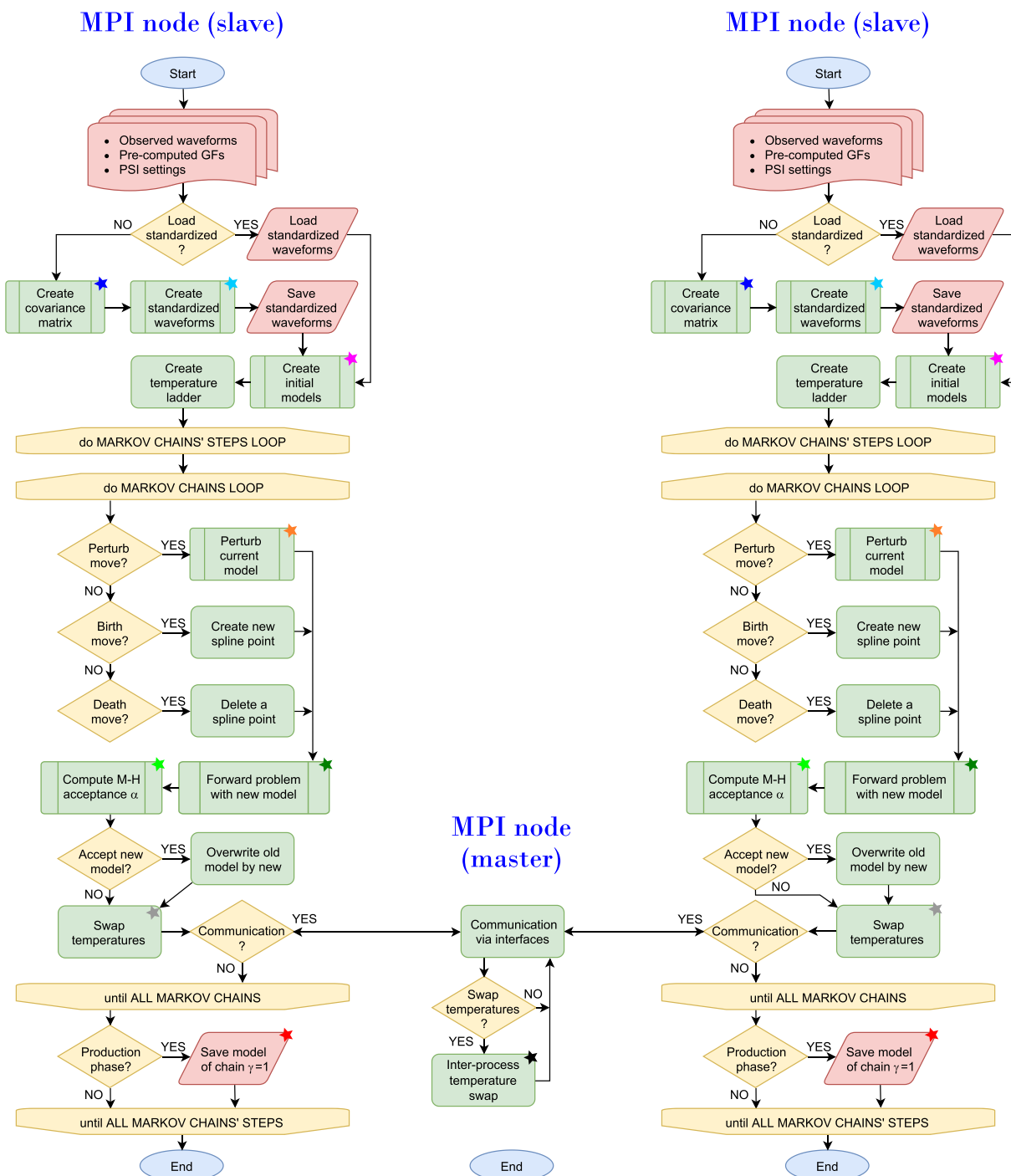


Figure 2. Flowchart diagram of the PSI's workflow. Arrows show flow order, red rhomboids indicate inputs and outputs, yellow diamonds are conditional operations, yellow horizontal bars show main loops, and green rectangles represent operations or subroutines. Small colored stars are anchors for text links (see text). The diagram shows the workflow on three MPI nodes (two slaves and one master) and their internode interaction.

Finally, PSI switches to the “production” phase, providing model samples drawn from the posterior trans-D PDF. The samples are saved by the “sampling” chains at temperature $\gamma = 1$ (red star in Figure 2). Arbitrary Markov chains are allowed to exchange their temperatures on intra-CPU and inter-CPU bases (silver and black stars in Figure 2, respectively) following the swap balance condition by Cambridge (2014). This phase lasts as many chain steps as necessary to create a sufficiently representative ensemble of solutions.

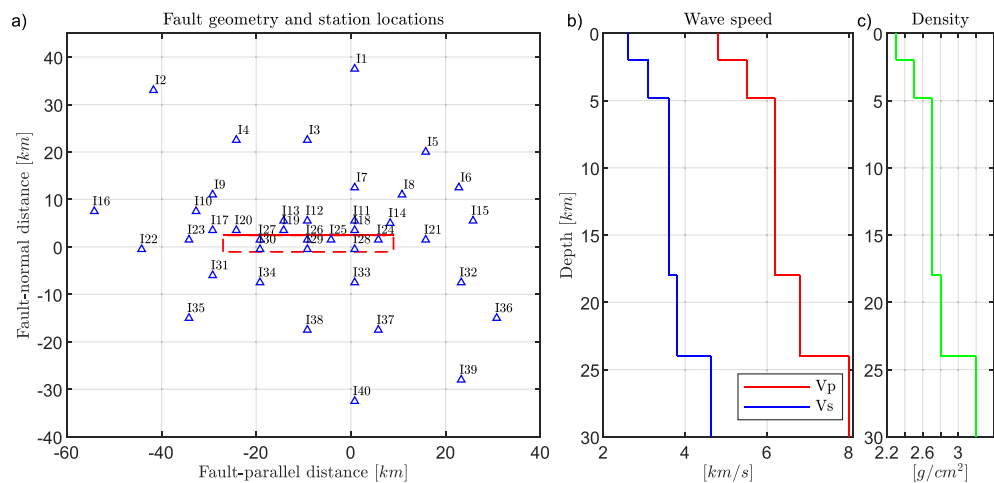


Figure 3. Settings of the synthetic SIV test *Inv1*. (a) Geometry of the fault (red rectangle) and station locations (blue triangles); (b) seismic wave velocities; and (c) density of the provided one-dimensional elastic layered medium.

To complete, the saved model samples from PSI are postprocessed by a Fortran90 code. It provides statistics (e.g., averages and occurrences in user-specified bins), the maximum likelihood model, and the maximum a posteriori (MAP) model estimate (see section 4.2).

4. Application to a Synthetic Test

We apply our methodology to community inversion benchmark *Inv1* from the SIV project (Mai et al., 2016, <http://equake-rc.info/SIV/>). The target source model is based on a spontaneous dynamic rupture simulation for an 80° dipping strike-slip fault. The reference model of $M_w6.6$ (seismic moment $\sim 1 \times 10^{19}$ Nm) has heterogeneous initial shear stress, depth-dependent normal stress, and smooth rupture termination. The fault has dimensions of roughly 30–35 km along the strike and 15–20 km downdip. The synthetic surface ground motion data at 40 sites (see Figure 3a) are provided with the nominal maximum resolved frequency of 2.5 Hz. We perform this benchmark using only the original synthetic waveforms, fault geometry, and one-dimensional velocity profile (Figures 3b and 3c) provided in the frame of the SIV exercise description.

4.1. Inversion Settings

We set the fault geometry following the description of the SIV test *Inv1* (see Figure 3 and Table 1). The fault is spatially discretized into 36×20 subfaults of size 1×1 km, that is, 720 subfaults in total. The strike and dip angles are fixed, while the rake angle, hypocenter position on fault, and the rupture initiation time are treated as unknowns (for details, see Table 1). The “observed” waveforms downloaded from the SIV project website were filtered between 0.05 and 0.5 Hz to use frequency band as utilized in the real data inversion. The GFs for all of the subfaults are precomputed by the discrete wavenumber method (Bouchon, 1981),

Table 1
Fault Geometry and Discretization of the SIV Test

	Value	Notes
Moment magnitude	$M_w6.6$	Seismic moment sought during inversion
Hypocenter depth	14 km	Hypocenter \mathbf{h} sought during inversion
Fault strike/dip	90°/80°	Fixed
Fault length/width	36 km/20 km	Fixed
Rake angle	180°	Rake θ_i sought during inversion
Subfault size	1 km × 1 km	$\Delta\Sigma$
Number of subfaults	720	N_Σ
Regular control points	13×7	Regular grid (Γ) along strike × dip

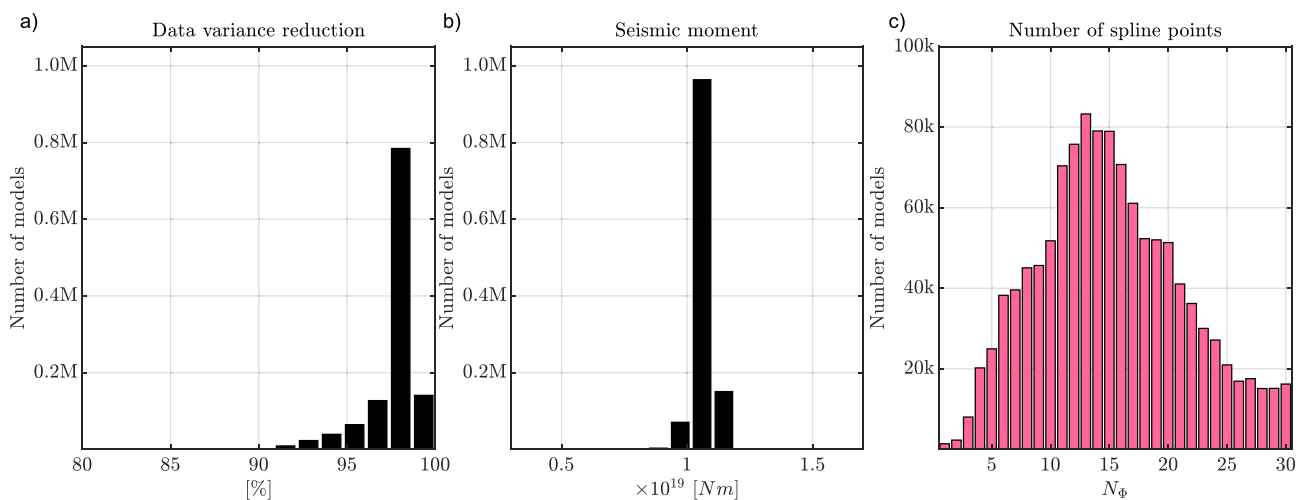


Figure 4. Statistics of the ensemble of all posterior slip models of the SIV test *Inv1*. (a) Histogram of standardized data variance reduction (100% = zero misfit of data and synthetics); (b) histogram of scalar seismic moments; and (c) histogram of the number of spline points in the models.

considering the given one-dimensional layered velocity model (Figures 3b and 3c). The data covariance matrix is computed prior to the inversion following the approach of Hallo and Gallovič (2016; ACF matrix).

We performed our nonlinear slip inversion (PSI) in parallel on 120 deployed CPU cores (119 slave and 1 master processes) of Xeon supercomputing cluster IT4I. There were 30 serial Markov chains processed by each CPU core with assigned temperatures. The utilized temperature ladder, with $\gamma \in [1, 50]$, has one sampling ($\gamma = 1$) and 29 exploration chains with γ drawn from a log-uniform distribution. The runtime was set to 48 hr (i.e., in total 5,760 CPU-hours; 3,451 exploration chains; and 119 sampling chains). For each of the 3,570 chains, the length of the burn-in and production phases were 1,000 and ~10,000 steps, respectively. In this test, PSI was able to visit ~37,000,000 of rupture models, and it produced ~1,200,000 slip model samples.

4.2. Inversion Results

The result of our Bayesian inversion is the ensemble of ~1,200,000 rupture models representing random draws from the posterior trans-D PDF. All the models in the ensemble have very high standardized data variance reduction (see Figure 4a), that is, standardized data fit, and hence, all models represent viable solutions in terms of fit with the observed waveforms. For source-scaling purposes, we define the total scalar seismic moment M_0 of the rupture models as

$$M_0 = \Delta \Sigma \sum_{i=1}^{N_\Sigma} \mu_i A_i, \quad (23)$$

where μ_i is shear modulus at the depth of i th subfault. The histogram of the inferred scalar seismic moment in Figure 4b has a sharp shape, being centered at 1.06×10^{19} Nm (i.e., M_w 6.6). Next, the histogram of the number of slip spline points of the ensemble models is shown in Figure 4c. The number of spline points is a nonphysical parameter; however, it is related to the spatial complexity of the slip distribution on the fault in our trans-D formulation. Note that initial slip models have assigned a single spline point ($N_\Phi = 1$) randomly generated on the fault. A new model with more spline points is more likely to be accepted if it improves the standardized data fit. However, an increment of the number of spline points is penalized by the higher dimensionality of the model space. This balancing mechanism works as an Occam's razor, where the spatial slip distribution is as simple as possible, but not simpler than as required by the waveform fits. This is the principle of our self-adapting inversion utilizing the trans-D formulation of the model space and the reciprocal distribution $p(N_\Phi) \propto N_\Phi^{-1}$ as Occam's razor (see supporting information Figure S1a).

Statistics of the ensemble of solutions are useful for the evaluation of model parameters' uncertainties in a real data case. Nevertheless, we would like to focus here in the synthetic test on the quality of a single

representative source model as it can be compared with the “target” (true) model. For example, we could look at the maximum likelihood solution, that is, the model with the highest standardized data variance reduction; see equation (10). Indeed, such a model would be representative in terms of data fit, but we prefer to inspect a representative model in terms of the posterior PDF; see equation (9). To find an estimate of the MAP model, we first determine the maximum of the marginal posterior probability of the number of slip spline points N_Φ (i.e., bin “13” in Figure 4c). Note that the posterior marginal probability on N_Φ is governed solely by the data misfit, and it is independent of individual posterior marginal PDFs of other parameters (see sections 2.4 and 2.5). Then, we search among the source models from this particular model space (i.e., all models with $N_\Phi = 13$) for the model with the highest standardized data variance reduction. Such a model is the MAP estimate as we utilized the efficiently homogeneous prior PDFs (assuming broad, physically acceptable values of the model parameters; see Appendix C). It is still only estimated as there is zero probability to hit precisely the target by the random exploration of the model space.

Our MAP slip model estimate for the SIV test *Inv1* has high data variance reduction of 99.1% (see the standardized data fit in Figure 5), has moment magnitude $M_w 6.6$ (seismic moment 1.07×10^{19} Nm), and consists of 13 spline points ($N_\Phi^{\text{MAP}} = 13$).

4.3. Comparison With the Reference Model

Here we compare the kinematic properties of our MAP model and the target model of the SIV test *Inv1*. The target kinematic model was created from the reference solution (Mai et al., 2016) by resampling into our discrete grid of subfaults’ size 1×1 km. The comparison of our MAP model and the target SIV model (used for computation of the synthetic data in the SIV project) is shown in Figures 6 and 7. First, the spatial distribution of slip on the fault (Figure 6a) fits quantitatively well with the reference (Figure 6b). The along-strike location of the asperity with the largest slip is also clearly resolved. The depth of the maximum slip area of this MAP model is shallower than that in the target SIV model. This issue may be related to the similar behavior of the standard L2-norm based inversions, where the observation data can be explained with a smaller amount of the slip on the shallow subfaults as they are closer to the stations on the surface. Moreover, as this is a noise-free synthetic test (data variance reduction ~99%), it could also be affected by the prior PDF on the slip, which is very weak but exists (see supporting information Figure S1d). Further, our method was able to resolve the location of the hypocenter on the fault (blue asterisk in Figure 6). The rake angles (slip directions) of our MAP model are similar to the reference model (blue arrows in Figure 6), especially in the high-slip areas. Contrarily, in the zones of small slip (white zones), the rake angles are scattered as small amplitudes of SRF suppress the influence of the rake angle on the resulting synthetic waveforms (see equation (3)). The latter applies implicitly also on the rise time, peak time, and rupture time values. Further, the rake angle exhibits some spatial symmetries (see Figure 6a). It is an artifact caused by almost identical GFs for neighboring subfaults. Hence, we can produce almost identical synthetic waveforms by using various combinations of rake angles at neighboring subfaults. Hence, it is advisable to use slip-weighted spatial means as a more robust representative value rather than isolated values of rake angle (and implicitly also rise time and peak time). We want to emphasize that this behavior is a common feature of slip inversions with spatially varying rake angle and it is not caused by our particular approach.

Figure 7 compares spatial distributions of slip rates of our MAP model (Figure 7a) and the target SIV model (Figure 7b). We also show temporal snapshots of the slip rates (Figures 7c and 7d, respectively) and SRFs from six selected points (Figure 7e) depicted by black stars in Figures 7a and 7b. The similarity of our MAP slip rate solution to the target SIV model is very satisfactory, especially when we consider that the original SRFs stem from a dynamic rupture simulation (Gallović et al., 2019a; Mai et al., 2016).

To conclude this section, our spatial-temporal parametrization of SRFs is sufficient for kinematic representation of earthquake sources, being compatible also with the basics of the rupture dynamics. Furthermore, the algorithm for the multidimensional model space exploration can produce a MAP model estimate that is close to the target model.

5. Application to the 2016 $M_w 7.1$ Kumamoto Earthquake

On 16 April 2016, Kumamoto prefecture in Kyushu region, Japan, was devastated by a shallow $M_{\text{JMA}} 7.3$ ($M_w 7.1$) earthquake. It generated destructive ground motions in the near-source region, causing severe

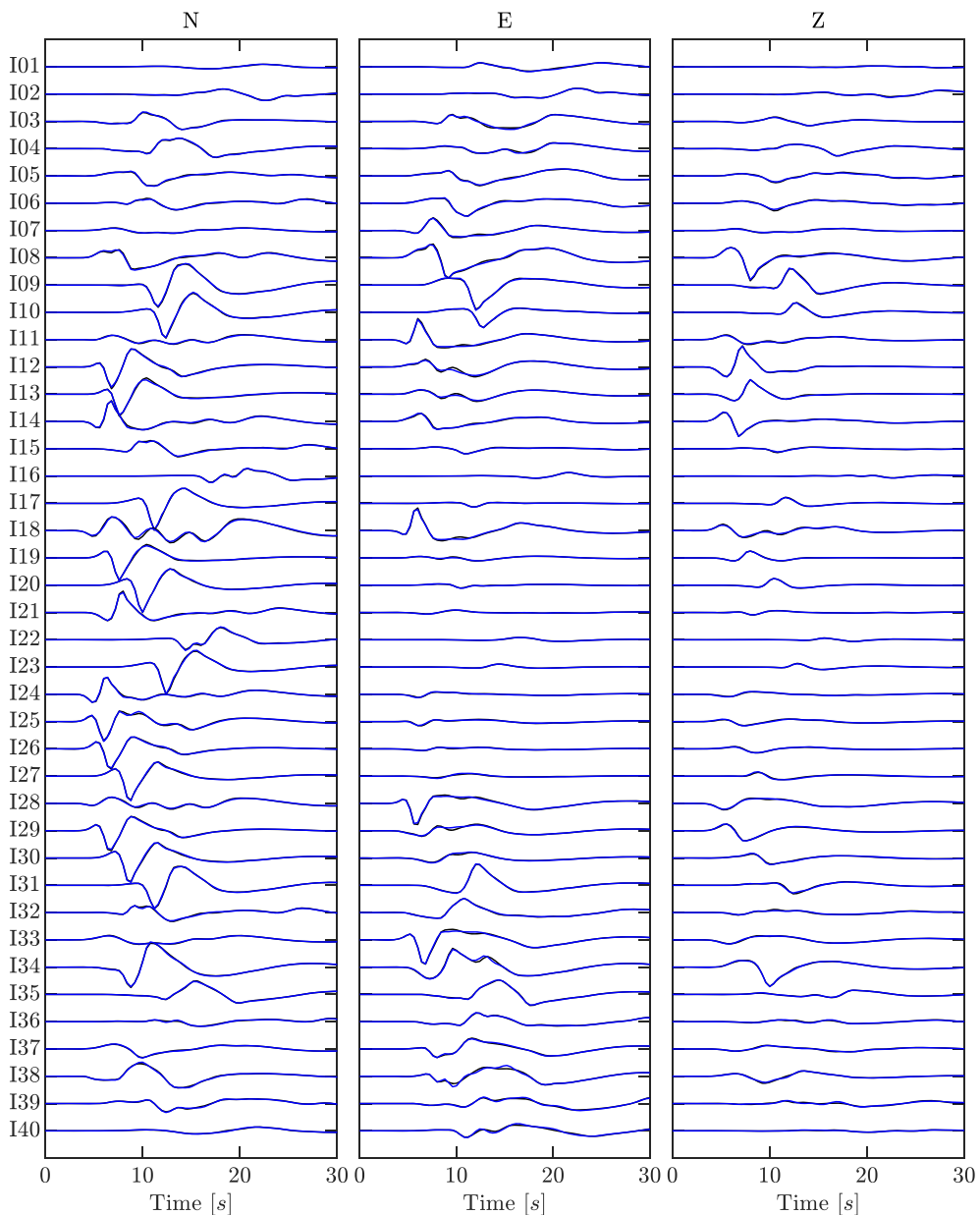


Figure 5. Fit of standardized “target” waveforms (black) by synthetics of the MAP model (blue) for the SIV test *Inv1*. Waveforms were filtered between 0.05 and 0.5 Hz before the standardization by the triangular matrix from the Cholesky decomposition of the covariance matrix (ACF matrix). The standardized waveforms are normalized by the largest amplitude over all stations and components. Note that the black curves are almost invisible as they are overlaid by the blue synthetics.

damage and 49 casualties. The mainshock occurred at 01:25 of Japan Standard Time (JST), that is, 28 hr after the first recognized foreshock of $M_{\text{JMA}} 6.5$, as reported by the Japan Meteorological Agency (JMA). It was followed by a series of weaker aftershocks of various locations and source mechanisms (e.g., Hallo et al., 2017; Kato et al., 2016). In the 2016 Kumamoto sequence, seven earthquakes reached or exceeded the instrumental intensity of lower 6 of the JMA intensity scale (0–7).

Fault slip source models for the mainshock were inverted from strong-motion records (e.g., Asano & Iwata, 2016; Kubo, Suzuki et al., 2016; Hao et al., 2017; Kobayashi et al., 2017; Yoshida et al., 2017). The inferred models suggest that the rupture started near the intersection of the Futagawa and Hinagu faults by right-lateral strike-slip movement, with subsequent propagation to the NE along the Futagawa fault as a

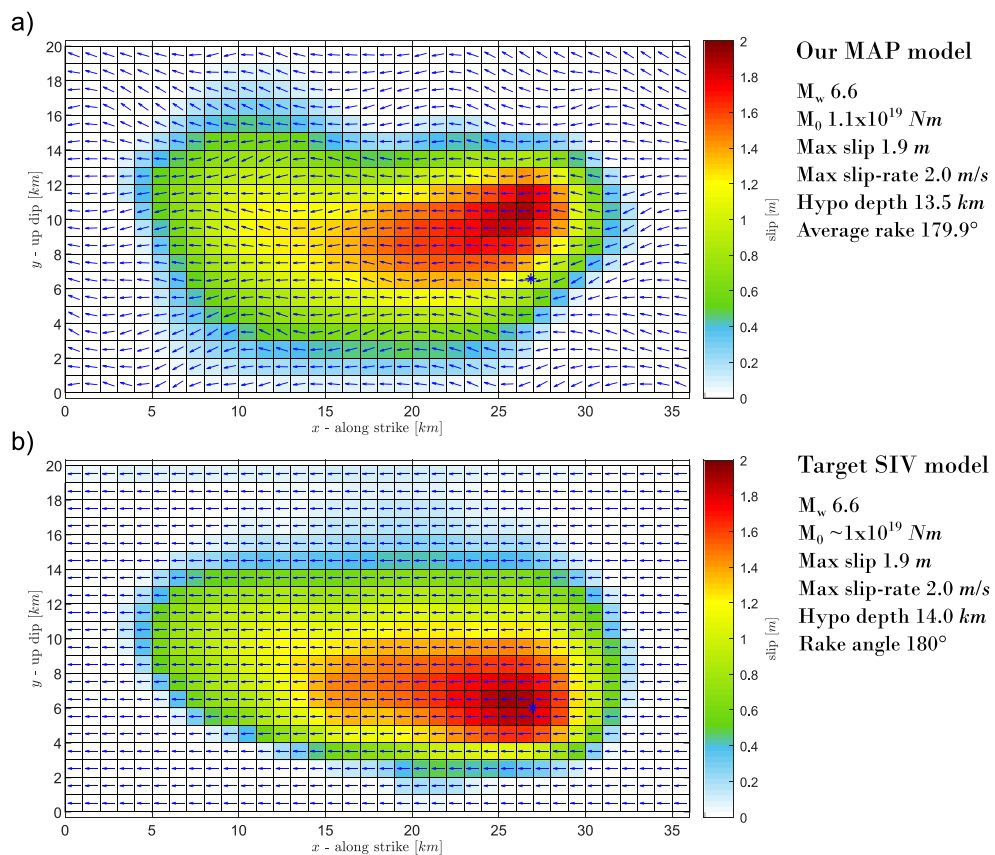


Figure 6. Comparison of the slip distribution of (a) our MAP model and (b) the target *Inv1* SIV model. The slip values are shown by color (see color bars). The rake angles (slip directions) are shown by blue arrows. The hypocenter position is shown by the blue asterisk. The fit of standardized waveforms for these MAP and target models is shown in Figure 5.

strike-slip with a normal faulting component. Common features of these fault slip models are consistent with field measurements of coseismic surface ruptures and static slip models from geodetic data (Fukahata & Hashimoto, 2016; Himematsu & Furuya, 2016). Nevertheless, detailed spatial-temporal distribution of slip on Futagawa and Hinagu faults may be biased due to the use of specific data, velocity model, method, constraints, and so on. Hence, we apply our Bayesian self-adapting fault slip inversion with GF uncertainty (PSI code) to discern reliable features of the present slip models for this earthquake.

5.1. Fault Geometry

Following Asano and Iwata (2016), we assume a fault plane model consisting of two planar fault segments based on surface traces of known active faults and the aftershock distribution (e.g., Kato et al., 2016). The first fault segment #1 is set along the Hinagu fault intersecting the hypocenter of the M_w 7.1 mainshock. The second (larger) fault segment #2 is set along the Futagawa fault spreading to NE from the intersection of both faults (see Figure 8). The Hinagu and Futagawa fault segments are assumed to have a rectangular shape of dimension larger than assumed by Asano and Iwata (2016) to not restrain the distance of the rupture propagation. For detailed settings of the assumed fault planes and spatial parametrization, see Table 2.

5.2. Data and Velocity Model

We use three-component waveforms recorded at 29 stations of the K-NET, KiK-net, and F-net strong-motion networks (Aoi et al., 2011; National Research Institute for Earth Science and Disaster Resilience [NIED], 2019a, 2019b; Okada et al., 2004) of the National Research Institute for Earth Science and Disaster Resilience, located up to the distance of 55 km from the mainshock epicenter (see Figure 8). The stations are selected based on distance and sufficient signal-to-noise ratio. Few regional stations were excluded from

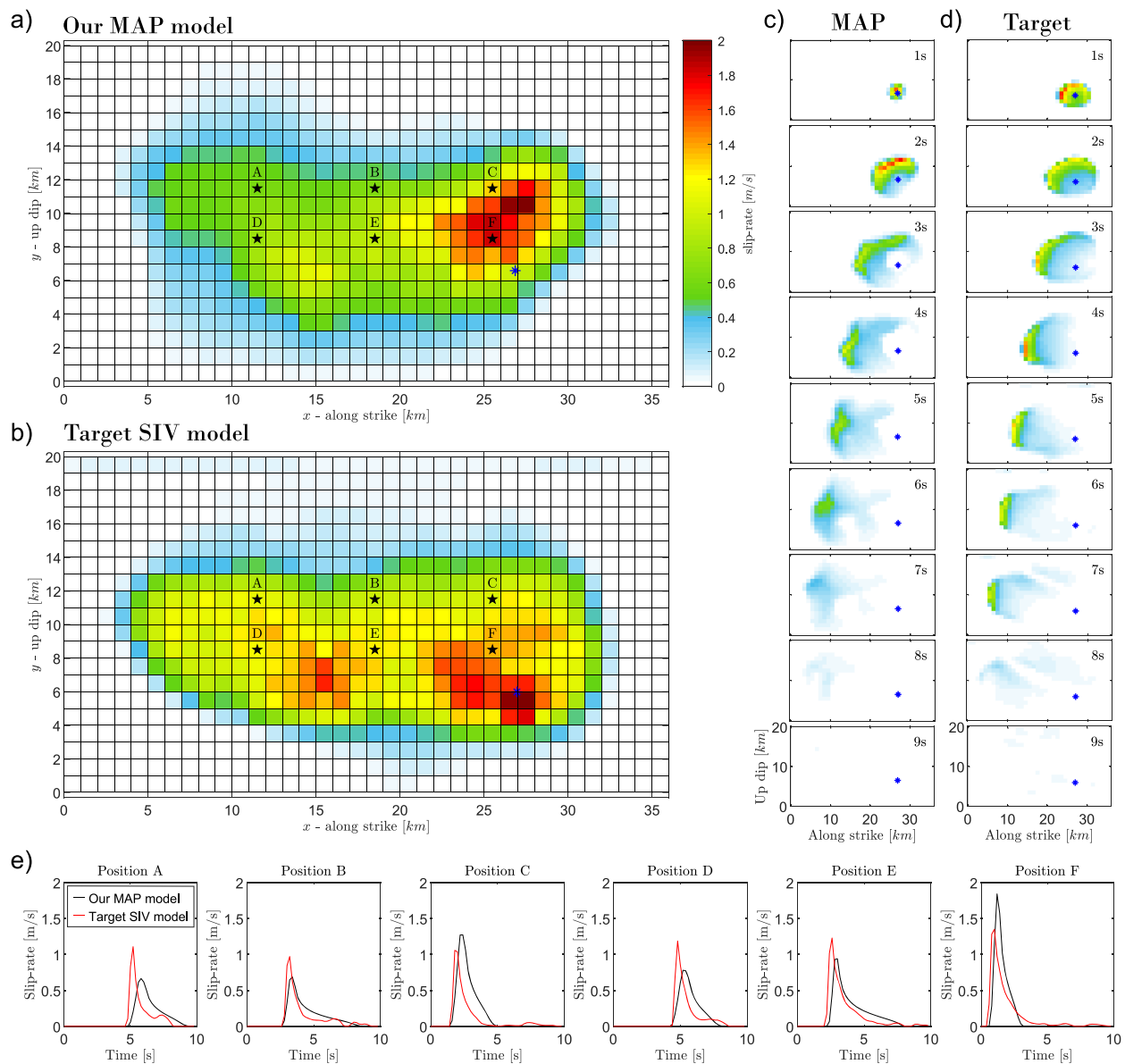


Figure 7. Comparison of slip rates of the MAP model and the target *Inv1* SIV model. The results are compared in terms of the spatial distribution of the peak slip rate for (a) our MAP and (b) the target model; slip rate time snapshots for (c) our MAP and (d) the target model; and (e) slip rate functions from six selected points depicted in panels (a) and (b) by black stars. The slip rate peaks in panels (a)–(d) are shown by color (see the common color bar). The hypocenter position is shown by the blue asterisk.

the selection, as their waveforms contain complex signals. Nevertheless, these stations are located on the edge of the area of interest (see gray triangles in Figure 8).

Original acceleration data (K-NET and KiK-net) and strong-motion velocity data corrected for the instrument response (F-net) are filtered by a band-pass filter at 0.05–0.5 Hz, and then they are integrated into displacements. The processed waveforms are downsampled to the sampling frequency of 2.5 Hz (0.4 s sampling interval) to reduce computational demands. The observed data time window used in the inversion spans 0–40 s after the origin time of the mainshock (Table 2).

We use one-dimensional station-dependent velocity models consisting of homogenous elastic layers for computing GFs. This way, we account for local thick near-surface sedimentary layers that might affect waveforms in the frequency range considered (0.05–0.5 Hz; Asano & Iwata, 2009). These one-dimensional velocity models (Figure 9) were extracted for every used station from the three-dimensional Japan

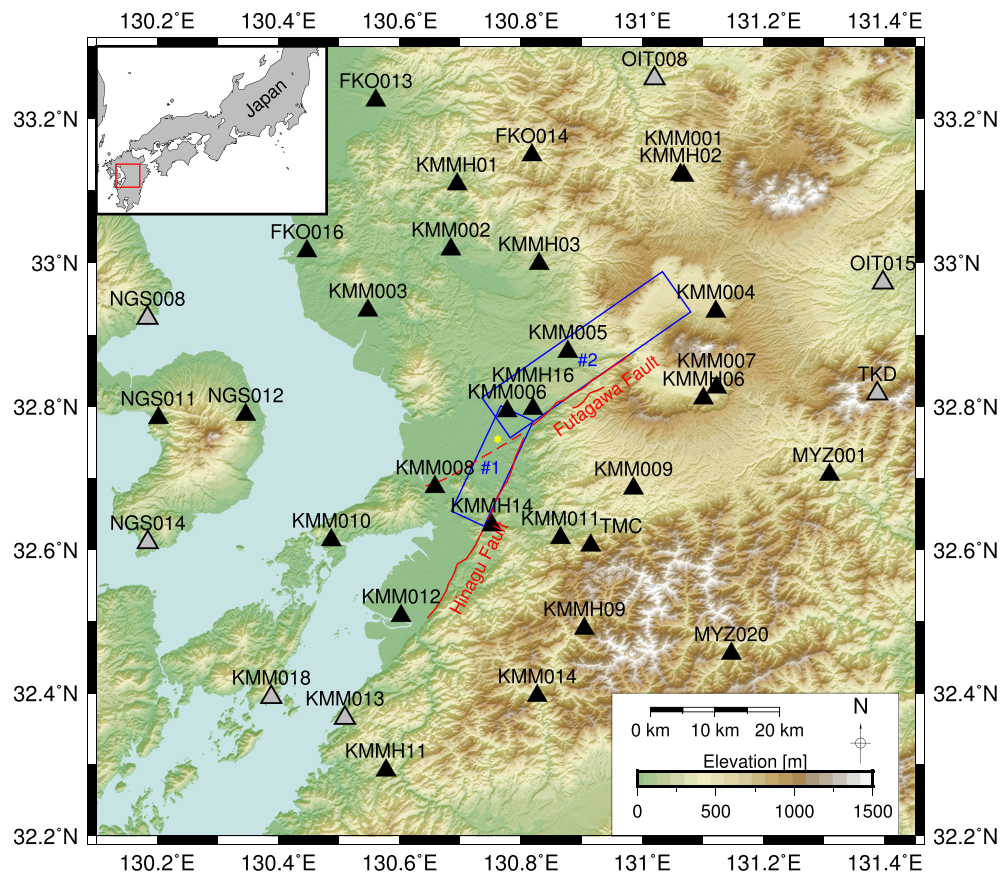


Figure 8. Map of the Kumamoto area with the settings of the M_w 7.1 earthquake inversion. Blue rectangles are Hinagu (#1) and Futagawa (#2) fault segments, yellow star is JMA epicenter, and triangles show positions of stations of the K-NET, KiK-net, and F-net networks that included in (black) or excluded from (gray) the inversion. Red lines denote surface traces of the main known active faults (e.g., Nakata & Imaizumi, 2002).

Integrated Velocity Structure Model (Koketsu et al., 2012) as velocity depth profiles below the particular receiver. To complete, for the sake of the computation of the scalar seismic moment M_0 in equation (23) (i.e., for estimation of the shear modulus μ_i on the fault), we use a one-dimensional velocity profile derived from the three-dimensional velocity model at the center position of the fault.

Table 2
Geometry and Discretization of the Hinagu and Futagawa Fault Segments

	Hinagu segment #1	Futagawa segment #2
Origin time ^a	16 April 2016/01:25:06 JST	16 April 2016/01:25:07 JST
Rupture initiation ^a	32.75°N/130.76°E/12 km	32.79°N/130.75°E/12 km
Fault strike/dip	205°/72°	235°/65°
Fault length/width	18 km/18 km	34 km/18 km
Rake angle ^a	-160°	-142°
Subfault size	2 km × 2 km	2 km × 2 km
Number of subfaults	81	153
Regular control points	7 × 7	13 × 7

Note. The rupture process is assumed to initiate formally at each fault segment separately; hence, they have independent rupture initiation points (formally a segment-specific hypocenter).

^aInitial model parameters, assumed free during inversion.

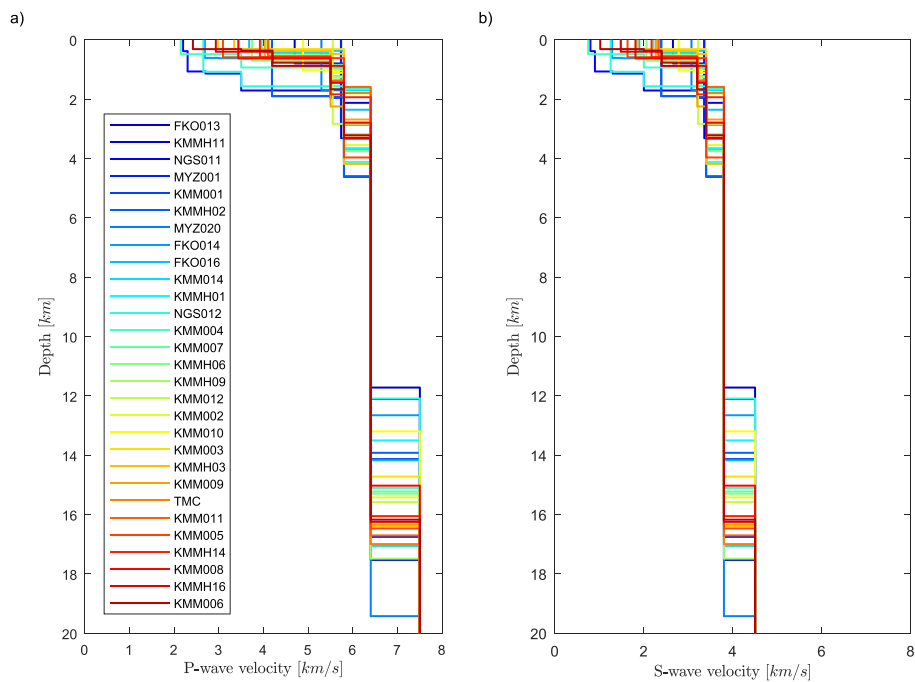


Figure 9. One-dimensional station-specific velocity models used in the inversion. (a) P wave and (b) S wave velocities of the layered models for the individual stations (for color, see legend). These models were extracted from the three-dimensional Japan Integrated Velocity Structure Model (Koketsu et al., 2012).

5.3. Inversion Settings and Procedure

In section 2 we describe parametrization and inversion of slip on a single fault segment. In the case of the two fault segments (#1 and #2), we consider the parametrization of the SRFs on each fault segment separately. The augmented trans-D model \mathbf{m} , initially formulated for a single segment and then for the two-segment model, reads

$$\mathbf{m} = (k^{\#1}, \mathbf{w}^{\#1}_{k^{\#1}}, k^{\#2}, \mathbf{w}^{\#2}_{k^{\#2}}). \quad (24)$$

It does not bring any additional constraints into our inverse problem formulation, and hence, the choice of a multiple-segment source model is straightforwardly implemented into the default PSI code. These two segments #1 and #2 are spatially discretized into 9×9 and 17×9 subfaults, respectively, of equal size of 2×2 km. The strike and dip angles are fixed, while the rake angles, rupture initiation point, and time are treated as unknowns (independently for each segment). Pairs of GFs for all of the assumed subfaults and receivers are precomputed by the discrete wavenumber method (Bouchon, 1981), considering the station-dependent velocity models in Figure 9. The data covariance matrix is computed before the inversion following the approach of Hallo and Gallović (2016; ACF matrix).

We performed our nonlinear slip inversion (PSI) in parallel on 360 deployed CPU cores (359 slave and 1 master processes) of Xeon supercomputing cluster IT4I. We used 30 serial Markov chains with the same temperature ladder settings as in the synthetic test. The runtime was set to 48 hr (i.e., in total 17,280 CPU-hours; 10,411 exploration chains; and 359 sampling chains). For each of the 10,770 chains, the length of the burn-in and production phases were 3,000 and $\sim 20,000$ steps, respectively. In the runtime, PSI visited $\sim 220,000,000$ models, and it produced $\sim 7,300,000$ rupture model samples representing random draws from the posterior PDF.

The standardized data variance reduction (i.e., standardized data fit) of all models from the ensemble is in the range of 73–79% (see the histogram in Figure 10a). The histogram of the inferred scalar seismic moment in Figure 10b is centered at 6.5×10^{19} Nm (i.e., $M_w 7.1$). The ensemble of solutions then suggests the seismic moment in the range of approximately $5.6 - 7.3 \times 10^{19}$ Nm (i.e., $M_w 7.1$ to $M_w 7.2$). Next, the histograms of the

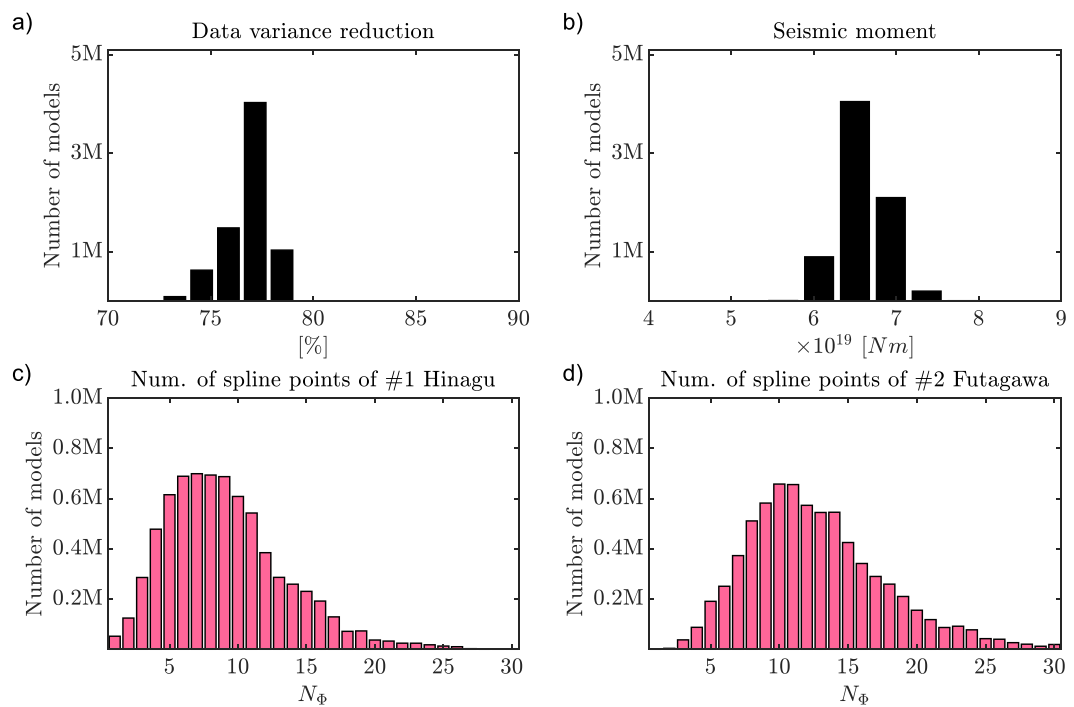


Figure 10. Statistics of the ensemble of all posterior slip models for the $M_w7.1$ Kumamoto earthquake. (a) A histogram of standardized data variance reduction; (b) a histogram of scalar seismic moments; (c, d) are histograms of the number of spline points describing the slip at the Hinagu (#1) and Futagawa (#2) fault segments, respectively.

total number of spline points of both fault segments are shown in Figures 10c and 10d. Those can be shown separately because each fault segment has its independent parameterization (see equation (24)). Thus, the resolved complexity of one fault segment is not bound to the second one. Such a feature is especially suitable in the case when one segment is dominated over by the second in terms of the released seismic moment. The 2016 Kumamoto mainshock is precisely such a case as the total slip on the Futagawa segment dominates over the total slip on the Hinagu segment (e.g., Asano & Iwata, 2016). Indeed, our statistics on the number of spline points suggest that PSI was able to resolve more complex spatial slip distribution (described by more spline points) on the dominant, larger Futagawa segment (Figure 10d) than on the smaller Hinagu segment (Figure 10c). We point out that the number of subfaults on the fault is not related to the spline points. Instead, the seismic moment of the segment controls the amplitude of the seismic waves and thus the segment's contribution to the data. The segment with weaker contribution thus has a weaker effect on the waveform misfit, and thus thanks to Occam's razor, more simple slip is preferred.

5.4. The MAP Model

The ultimate result of our Bayesian inference of the $M_w7.1$ Kumamoto earthquake kinematic rupture model is the ensemble of possible models drawn from the posterior PDF. Nevertheless, we would like to focus on the MAP model estimate first, as it allows direct comparison with other proposed rupture models for the 2016 Kumamoto earthquake. We use the model with the highest standardized data variance reduction from models having $N_\Phi^{#1} = 7$ and $N_\Phi^{#2} = 10$ (see maxima in Figures 10c and 10d) as the MAP model estimate (see section 4.2 for details). Our MAP model has data variance reduction of 78.2% and the scalar seismic moment of $6.8 \times 10^{19} \text{ Nm}$ ($M_w7.15$). The spatial slip distribution is shown in Figure 11a. Figures 11b and 11c show the spatial distribution of peak slip rates and slip rate snapshots, respectively.

The MAP model has hypocenter (i.e., the early rupture initiation point from our low-frequency data) located at the Hinagu segment at a depth of 10 km (blue asterisk on #1 in Figure 11). The rupture propagates by an average rupture velocity of 2.5 km/s along this segment (see #1 in Figure 11c), terminating at the intersection with the Futagawa segment. Large slip on the Hinagu segment is concentrated in the zone between the

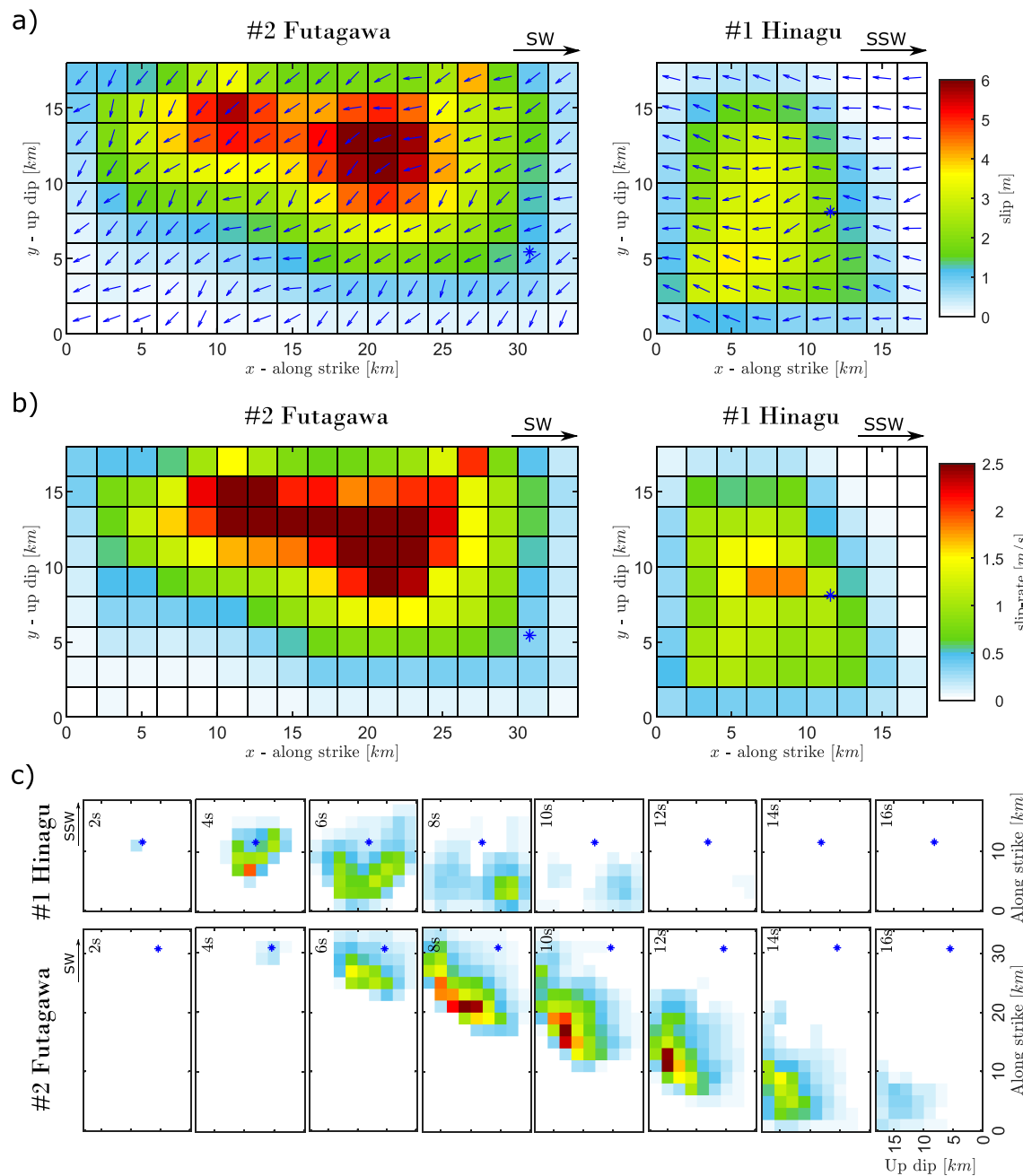


Figure 11. The MAP model for the $M_w 7.1$ Kumamoto earthquake. (a) The spatial slip distribution (see slip color bar). Rake angles (slip directions) are shown by blue arrows. (b) The spatial distribution of peak slip rate and (c) the temporal slip rate snapshots. Slip rate amplitudes are shown by color (see slip rate color bar common to panels b and c). The segment-specific rupture initiation points are shown on both segments #1 and #2 by blue asterisk.

hypocenter and the intersection with the Futagawa segment at a depth of approximately 8–14 km. The inferred rupture initiation time on the Futagawa segment is delayed by 1.5 s with respect to the origin on the Hinagu segment and is located at a depth of approximately 12.5 km close to the intersection of both segments (blue asterisk on #2 in Figure 11). The rupture continues along the Futagawa segment upward and to NE by an average rupture velocity of 2.8 km/s (see #2 in Figure 11c). The largest slip on the Futagawa segment is concentrated at shallower depths of approximately 1–8 km (see #2 in Figure 11). Eventually, the rupture terminates at shallow depths inside the Aso volcano caldera (i.e., NE edge of segment #2). The inferred rake angles on the Hinagu segment indicate dominating right-lateral strike-slip

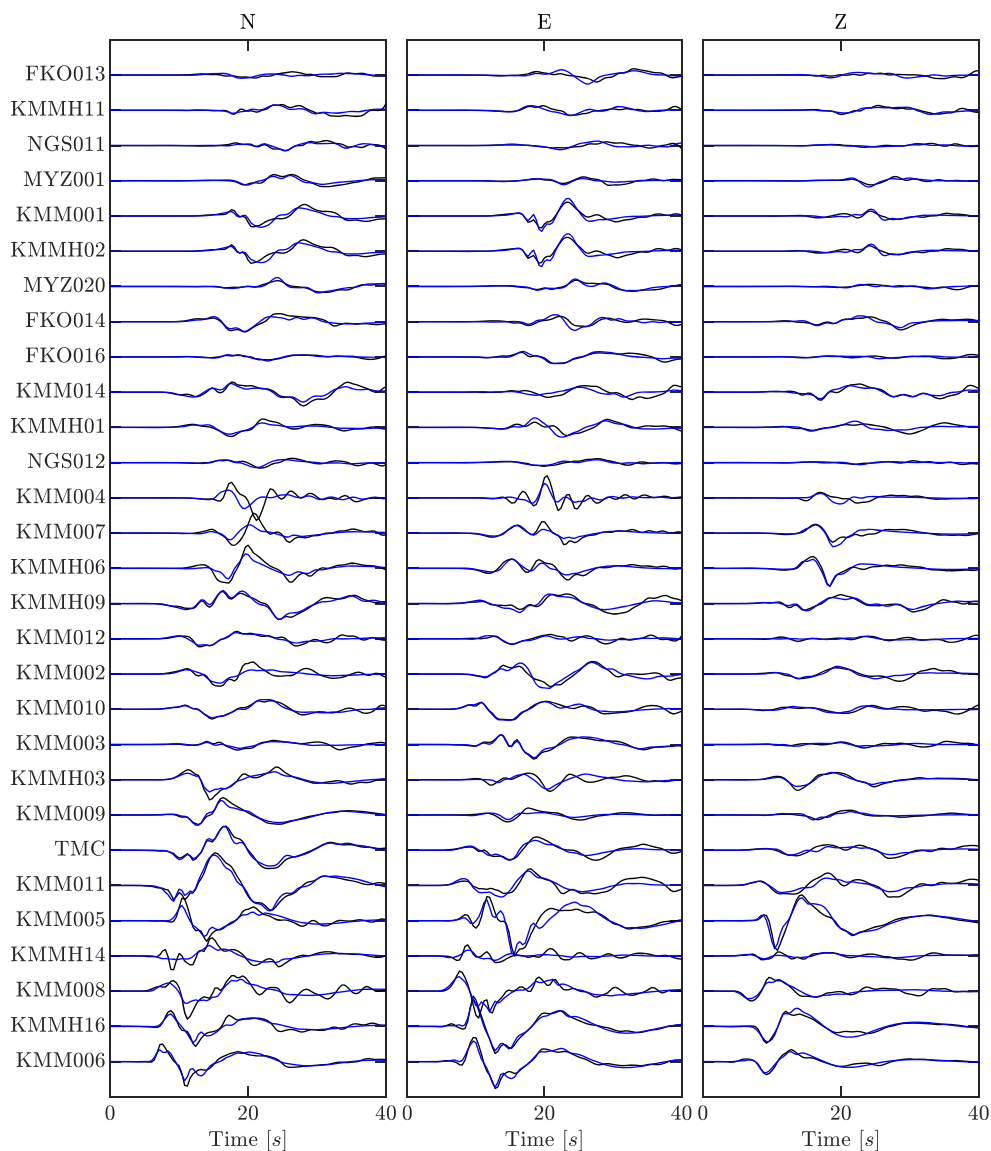


Figure 12. Comparison of standardized observed waveforms (black) and synthetics for our MAP model (blue) of the M_w 7.1 Kumamoto earthquake. Waveforms were filtered between 0.05 and 0.5 Hz before the standardization by triangular matrix from the Cholesky decomposition of the covariance matrix (ACF matrix). Variance reduction is 78.2%. In the plot, the standardized waveforms are normalized to the largest value over all the stations and components.

shear (see #1 Figure 11a). Contrarily, the slip directions on the shallow part of the Futagawa segment have a significant normal-slip component (see #2 Figure 11a).

To quantify the data fit of this MAP model, we use a misfit function computed from the standardized residuals, that is, waveforms multiplied by the triangular matrix from the Cholesky decomposition of the data covariance matrix (see equation (12) and Hallo & Gallović, 2016). In such formulation, the standardization amplifies the low-frequency part of the spectrum for stations at intermediate distances, which enhances their weight in the inversion. Figure 12 shows the fits of the standardized waveforms for our MAP model.

5.5. Ensemble Statistics

The ensemble of $\sim 7,300,000$ possible slip models allows statistical evaluation of the inferred model parameters and an assessment of the source model uncertainty. Hence, we can look critically in this section on the MAP model as merely a single representation of the many plausible slip models.

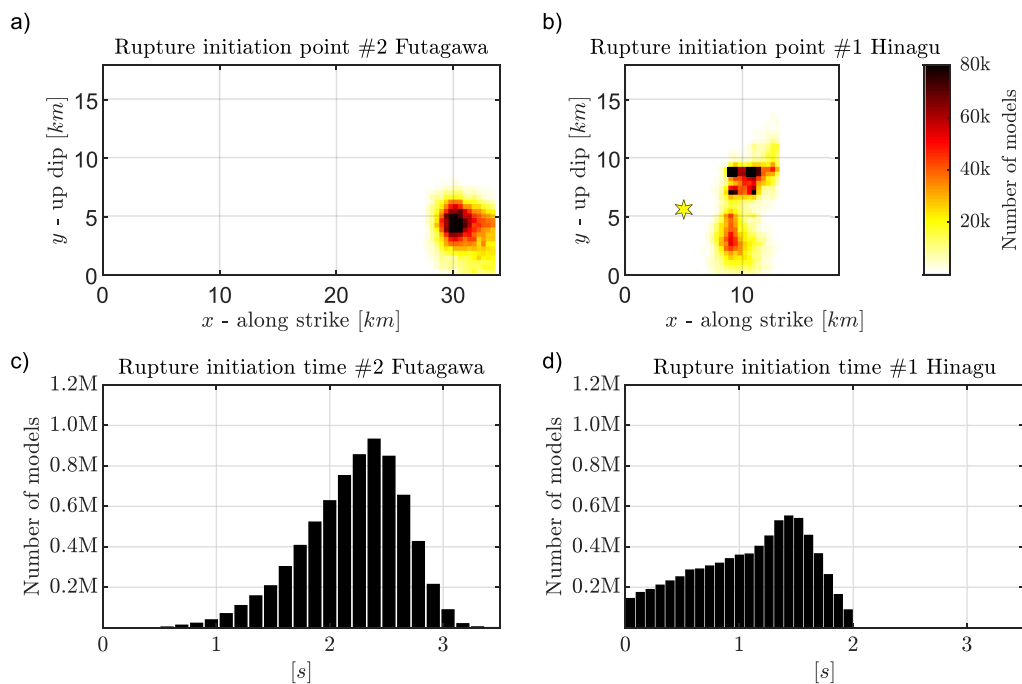


Figure 13. Ensemble statistics of rupture initiation of the source models for the $M_w 7.1$ Kumamoto earthquake inferred from low-frequency data. (a, b) Statistics of the rupture starting point (see color bar). (c, d) Histograms of the rupture initiation time from the reference time at 0.0 s. The statistics are created for both the Hinagu (#1) and Futagawa (#2) fault segments. Star denotes the JMA hypocenter.

First, we evaluate the uncertainty of the rupture initiation point and time on both fault segments (Figure 13). The rupture initiation position and time are better resolved on the larger, dominant Futagawa segment (Figures 13a and 13c) than on the smaller Hinagu segment (Figure 13b and 13d). The initiation point on the Futagawa segment is located at the depth of approximately 11–16 km close to the intersection of both segments (Figure 13a), while the initiation point on the Hinagu segment is rather uncertain (especially in its depth) as manifested by its complex marginal posterior PDF (see Figure 13b). Still, the JMA hypocenter on the Hinagu segment is close to the higher posterior PDF on the rupture initiation as inferred from our low-frequency data. Next, the rupture initiation time on the Futagawa segment is distinctly delayed with respect to the Hinagu segment (see histograms in Figures 13c and 13d). Still, the exact value of this delay is hard to judge due to the significant uncertainty of the rupture initiation time on the Hinagu segment. The whole ensemble supports the rupture initiation properties as captured by the MAP model.

As observed for the MAP model, the rise time, peak time, and rake angle vary significantly along the fault due to their spatial trade-offs (see also section 4.3). Hence, we use slip-weighted spatial averages as representative values for each model from the ensemble. The slip weighting is used so that the subfaults with negligible SRF amplitudes (being thus practically unconstrained) are suppressed in the statistics. Histograms of such weighted averages are shown in Figure 14 for both fault segments. The statistics for the Hinagu segment (#1; Figures 14a, 14c, and 14g) reveals that SRFs have an average rise time of 4.0–5.8 s, an average peak time of 1.4–1.7 s, and an average rake angle of $-180^\circ \pm 5^\circ$. For the Futagawa segment (#2; Figures 14b, 14d, and 14h), SRFs have an average rise time of 3.6–5.2 s, an average peak time of 1.3–1.6 s, and an average rake angle in the range from -145° to -150° . The inferred rake angles support slip model with right-lateral strike-slip shear movement on the Hinagu segment and significant normal-slip component on the Futagawa segment, as also present in our MAP model. To complete, Figures 14e and 14f show histograms of slip-weighted averages of the rupture velocities for both fault segments. They are below the S wave speeds, so there is no evidence of supershear rupture propagation along the segments.

To show the statistics and uncertainties of the spatial distribution of slip (or slip rate) in a concise graphics, we introduce here a modified polar histogram plot and denote it as the “ring polar histogram” (RPH).

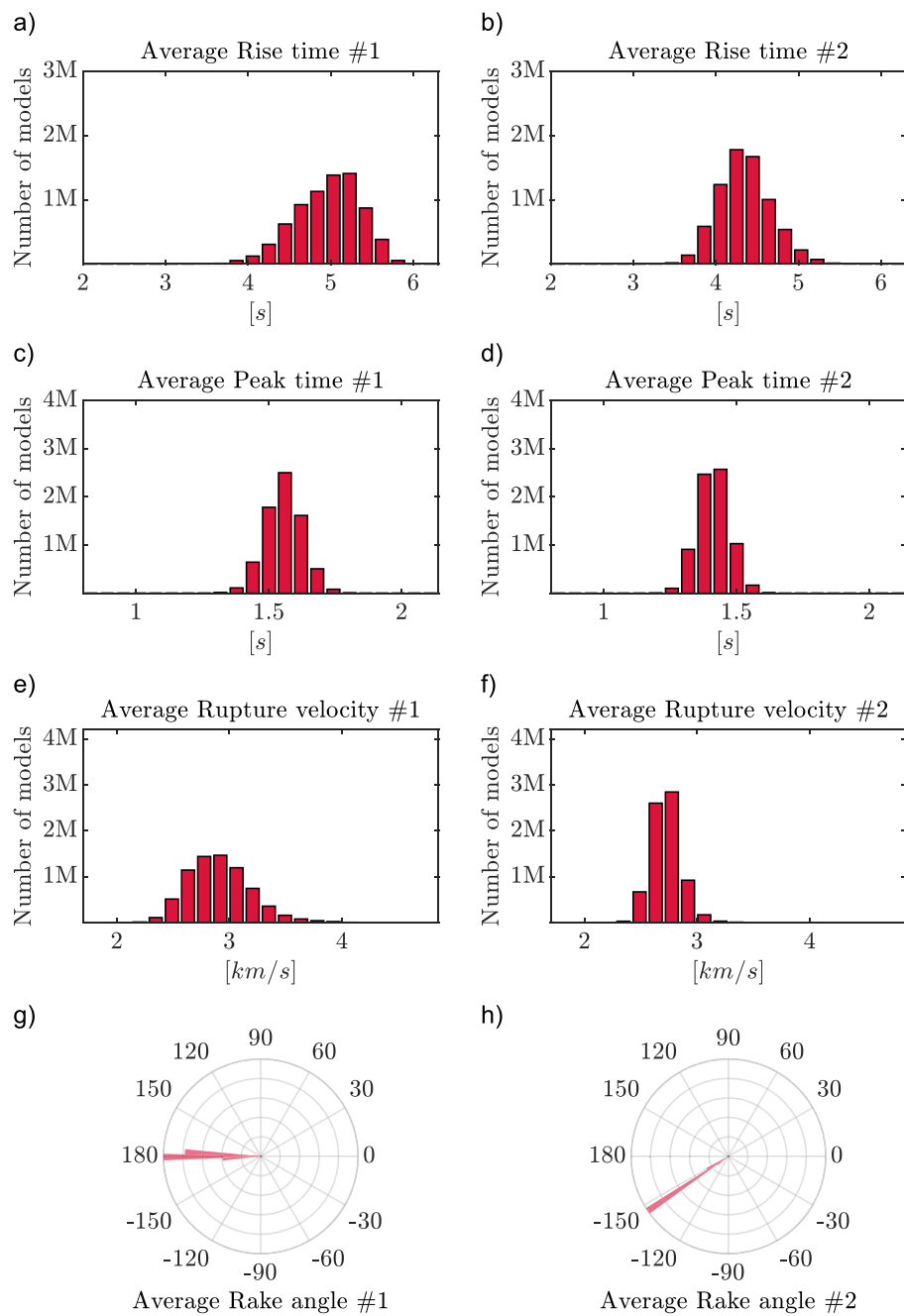


Figure 14. Statistics from the ensemble of source models for the M_w 7.1 Kumamoto earthquake plotted as histograms of slip-weighted spatial averages of the (a, b) rise times, (c, d) peak times, (e, f) rupture velocity, and (g, h) rake angles. The statistics are created for the Hinagu (#1) and Futagawa (#2) fault segments individually (left and right, respectively).

The RPH is a radially symmetric polar plot (see three examples in Figure 15d) designed for graphical representation of a random variable with spatially varying statistical properties (e.g., mean and standard deviation). In our particular case, the radial coordinate of the RPH has the meaning of slip (or slip rate) value on a specific subfault. The angular coordinate of RPHs has no meaning, and hence, the RPHs are radially symmetric for better visualization. The radial coordinate is divided into several equal-width value bins (i.e., histogram bins) so that each bin can be represented by an equal-width hoop of the various radii. All hoops have assigned a color based on the occurrence of the slip (or slip rate) value within the given

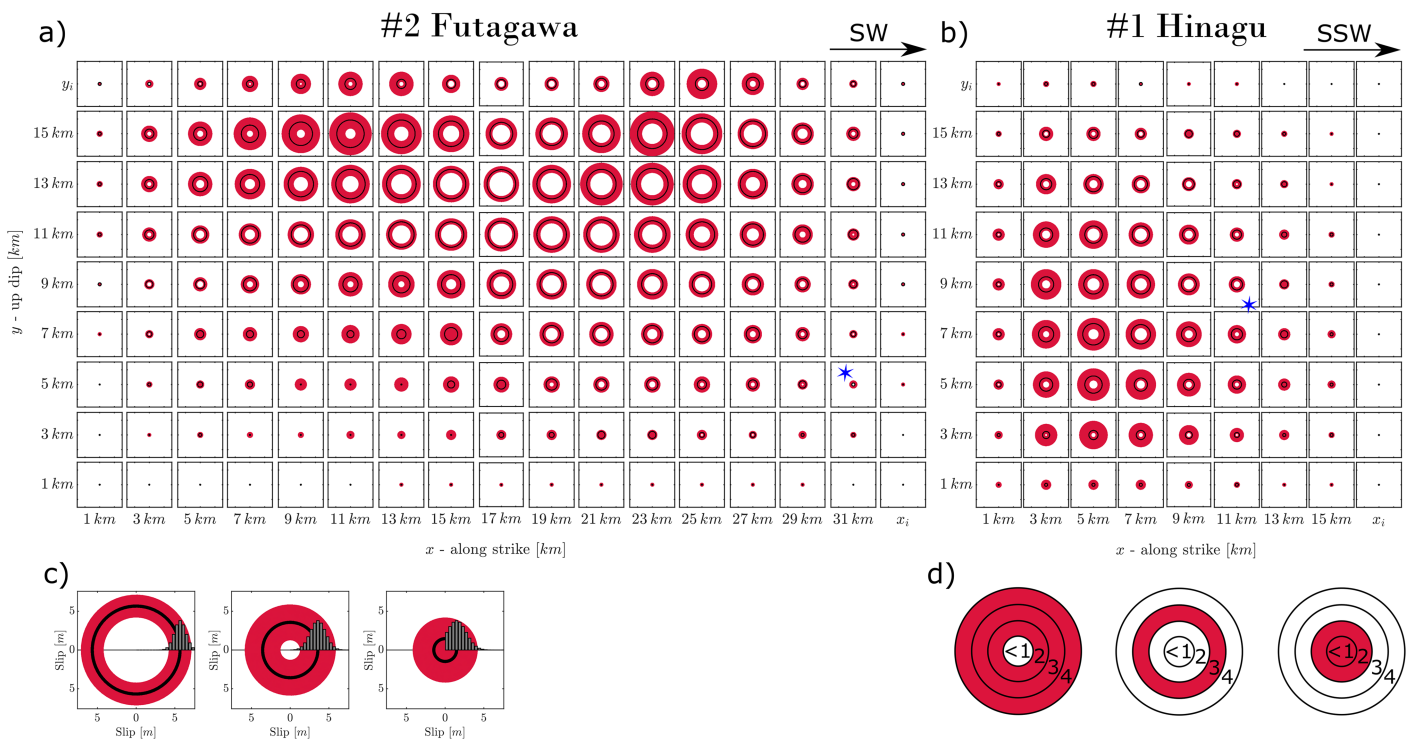


Figure 15. Ring polar histogram (RPH) plots of slip values of the $M_w7.1$ Kumamoto earthquake. The RPH plots of slip are shown for all subfaults distributed along strike and dip of the (a) Futagawa (#2) and (b) Hinagu (#1) fault segments. (c) Legend to the RPH plots in (a) and (b) as all subplots share axes limits. The segment-specific rupture initiation points of the MAP model are shown by the blue asterisks for reference. (d) Three illustrative RPH plots (see text). The red disk thickness has the meaning of uncertainty, and the hoop with the maximum posterior marginal probability is highlighted by black color.

bin in the solution ensemble. The hoops (i.e., bins) with occurrence exceeding the threshold of 10% of maximum count from all bins are filled by a color (red for slip in Figure 15; blue for slip rate in Figure 16); otherwise, the hoops are left white (transparent). Typically, the colored hoops then form a ring. This ring shows the range of plausible values by its inner and outer margins, as captured by the whole ensemble of solutions. The width of the compact ring in RPH shows an estimate of the uncertainty. If the center $[0, 0]$ of the RPH is filled by color, the plausible slip values from the ensemble also encompass zero (Figure 15d). These RPH plots are plotted for each subfault (Figures 15a and 15b), showing the spatial variations of the statistical properties of the slip (or slip rate) along the fault. To complete, a hoop representing the maximum posterior marginal probability (i.e., histogram bin with maximal model count) is painted in black (see Figure 15c).

The RPH plots of slip from our ensemble of models for the $M_w7.1$ Kumamoto earthquake are shown in Figure 15. The large slip zone on the Hinagu segment (#1; Figure 15b) at a depth of 8–14 km exhibits considerable uncertainty. Hence, the slip value can be smaller in this zone than suggested by the MAP model (#1 in Figure 11a). On the other hand, the low slip value in the southernmost part of the Hinagu segment is a feature supported by the whole ensemble of slip models (#1; Figure 15b). The RPH plot for the Futagawa segment (#2; Figure 15a) shows maximum slip having values in the range of 4–8 m. The slip value is well resolved in the central and southwestern zone (thin, large red rings), while it has significant uncertainty in the shallow and deep northeastern zone (very thick red rings).

Figure 16 (blue rings) shows RPH plots of peak slip rates and temporal slip rate snapshots. The latter indicates that the rupture propagation pattern, as described by the MAP model, is a well-resolved feature consistent across the whole ensemble of solutions.

5.6. Critical Assessment of Our Slip Model and Comparison With Other Studies

Major characteristics of our MAP model and statistics from the ensemble suggest the following scenario of the rupture process of the 2016 $M_w7.1$ Kumamoto earthquake. The rupture started on the Hinagu fault by

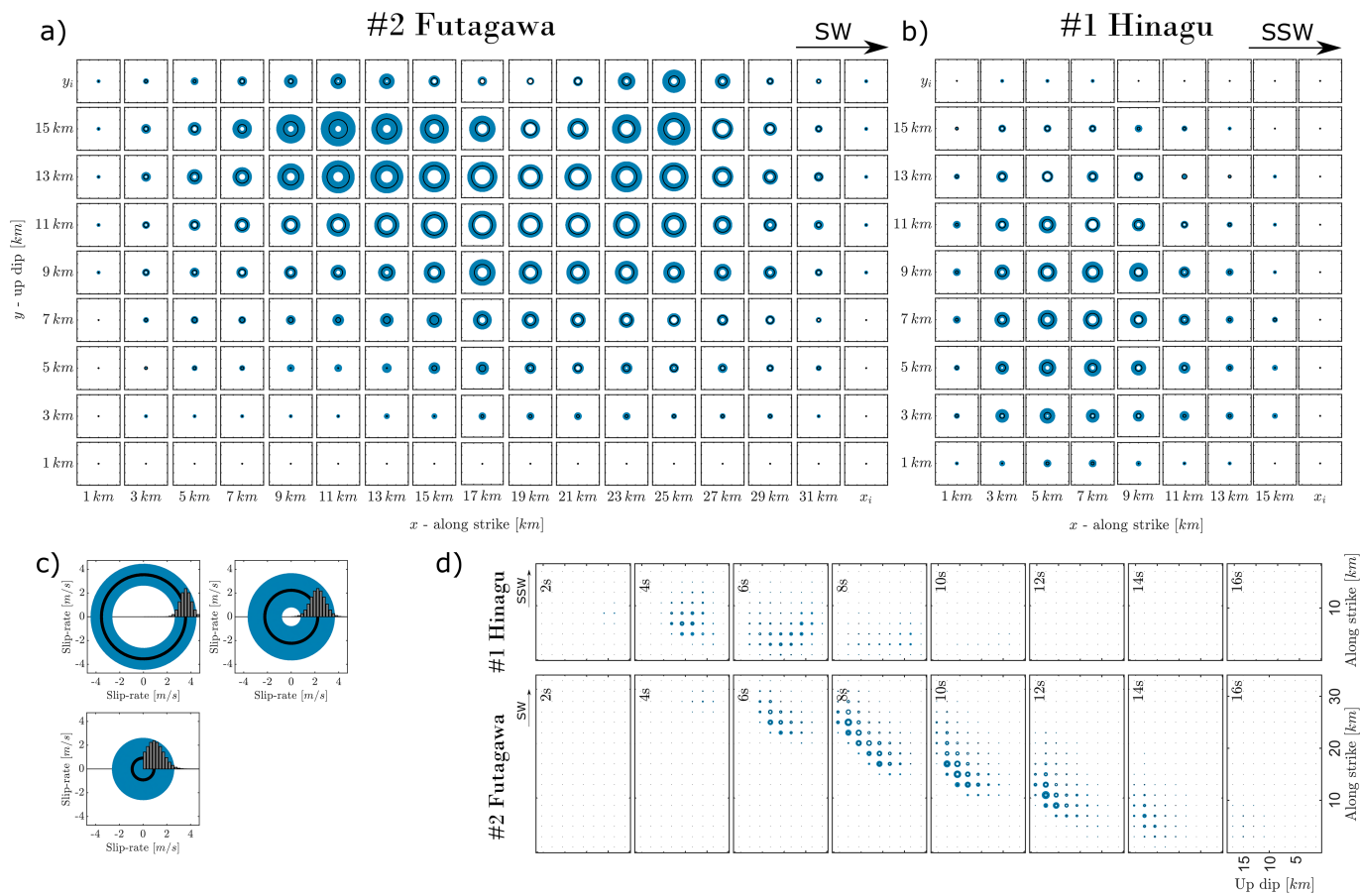


Figure 16. Ring polar histogram (RPH) plots of slip rates of the $M_w 7.1$ Kumamoto earthquake. The RPH plots of peak slip rates are shown for all subfaults of the (a) Futagawa (#2) and (b) Hinagu (#1) fault segments. (c) Legend to the RPH plots as all subplots share the same axis limits. (d) RPH plots of temporal slip rate snapshots (statistics of slip rates at a given time). The blue disk thickness has the meaning of uncertainty, and the hoop with the maximum posterior marginal probability is highlighted by black color.

a right-lateral strike-slip shear movement and propagated along the Hinagu fault, reaching the intersection of the Hinagu and Futagawa faults. The initiation point of the rupture on the Futagawa fault is located at the intersection of both faults at the depth of approximately 11–16 km. Then the rupture propagated upward and to NE along the Futagawa fault as a strike-slip with a normal faulting component. The largest slip of 4–8 m took place on the Futagawa fault. The duration of the whole rupture process is estimated to be approximately 16 s. We point out that these results are in accord with previous studies of this event (e.g., Asano & Iwata, 2016; Kubo, Suzuki et al., 2016; Yoshida et al., 2017; Himematsu & Furuya, 2016).

The inferred scalar seismic moment of our slip models is in the range of $5.6\text{--}7.3 \times 10^9$ Nm. These values are larger than the seismic moment obtained by Asano and Iwata (2016), that is, 4.5×10^{19} Nm ($M_w 7.0$), or by Yoshida et al. (2017), that is, 4.7×10^{19} Nm ($M_w 7.1$). Nevertheless, the lower limit of our estimate is close the scalar seismic moment obtained by Kubo, Suzuki et al. (2016), that is, 5.5×10^{19} Nm ($M_w 7.1$). The somewhat larger seismic moment may be caused by a larger assumed fault in our models, which would be in agreement with Yoshida et al. (2017), who obtained seismic moment 6.7×10^{19} Nm ($M_w 7.2$) before trimming their slip model.

Ensemble statistics proved that the right-lateral strike-slip shear movement on the Hinagu fault and the strike-slip with a significant normal-slip component on the Futagawa fault are well-resolved features of this earthquake. Indeed, such slip directions are also presented by other authors (Asano & Iwata, 2016, Kubo, Suzuki et al., 2016, and Yoshida et al., 2017). Further, the so-called RPHs showing spatially varying statistical properties of slip (Figure 15) show the following:

- The southernmost zone of the Hinagu segment (#1) is characterized by lower slip than that on the Futagawa segment (#2), as also inferred by the other studies.
- Our inferred solutions show high uncertainty of the slip on the Hinagu segment (#1). This is in accord with the variability of solutions of the other authors. Asano and Iwata (2016) located a slip asperity at shallow depth, while models by Kubo, Suzuki et al. (2016) and Yoshida et al. (2017) resolved it less pronounced and located at a slightly different position on the Hinagu fault.
- The large slip asperity in the southwest and central part of the Futagawa fault (#2) is inferred with rather low uncertainties in our inversion. Hence, it can be considered as a well-resolved feature, being also consistently imaged by the other studies.
- We consider slip at shallow depth northeast on the Futagawa fault (#2) to be uncertain. Indeed, Asano and Iwata (2016) and Yoshida et al. (2017) inferred only insignificant slip, while Kubo, Suzuki et al. (2016) inferred significant slip for this shallow zone.

6. Discussion and Conclusions

We have developed a novel Bayesian kinematic slip inversion, which can account for the uncertainty of GFs as the dominant source of variability of the solutions. Our nonlinear slip inversion method relies on a self-adapting spatial parametrization of SRFs using a varying number of spline control points on the assumed fault (e.g., Causse et al., 2017). The temporal parameterization utilizes the regularized Yoffe function (Tinti et al., 2005). The GF uncertainties are included in our formulation using full data covariance matrices composed from approximate covariance functions introduced by Hallo and Gallović (2016). Triangular matrices from the Cholesky decomposition of the covariance matrices then allows working with standardized waveforms, which reduces computational demands on solving the inverse problem. We note that other sources of uncertainty (e.g., fault geometry as proposed by Ragon et al., 2018, 2019; or propagation inaccuracies as addressed by Spudich et al., 2019) might be implemented in the trans-D formulation as well by considering the appropriate covariance matrix. Further, inference of the fault geometry might be implemented also following Shimizu et al. (2020) by assuming variable subfaults' strike and dip angles, by dealing with GFs for five basic double-couple components of subfaults' moment tensors.

Our representation of the SRFs consists of a varying number of parameters, and hence, our posterior PDF on model parameters consists of a varying number of dimensions. Hence, we utilize the multiple-state formulation of the posterior PDF following Green (1995). The posterior PDF is then sampled by trans-D MCMC algorithm with implemented reciprocal Occam's razor. The developed computational code utilizes very efficient PT (Cambridge, 2014) working on multiple MPI nodes so that it can be run on supercomputing clusters as well as on personal computers. The PSI program including its source code is available under the GNU General Public License for free for noncommercial use.

The application to synthetic SIV test *Inv1* demonstrates that our spatial-temporal parametrization of SRFs is suitable for kinematic representation of earthquake sources, being compatible also with the basics of rupture dynamics. Furthermore, the utilized algorithm for the multidimensional model space exploration is capable of an effective exploration of a model space of several hundreds of dimensions. The number of dimensions of the models is linearly related to the number of used spline control points, which is linked with the potential spatial complexity of the slip distribution on the fault. The increase in the number of dimensions allows obtaining more complex slip models, which is, however, penalized. Such a balance mechanism of our self-adapting inversion works effectively as Occam's razor, where the spatial slip distribution is as simple as possible, but not simpler than required by the waveform fits.

Our Bayesian slip inversion is applied to the destructive 2016 M_w 7.1 Kumamoto, Japan, earthquake from 16 April. The fault geometry consists in this case of two separate fault segments, where slip on the larger one dominates over the slip on the smaller segment (e.g., Asano & Iwata, 2016). We utilize the self-adapting mechanism separately at each fault segment (independent parameterization for both segments) to not bound resolved spatial complexities of their slip. Indeed, our statistics of the number of spline points from the ensemble of ~7,300,000 models suggests that we were able to resolve more complex spatial slip distribution on the dominant, larger, Futagawa segment.

Major characteristics of our slip model and statistics from the ensemble are in accord with previous studies (e.g., Asano & Iwata, 2016; Kubo, Suzuki et al., 2016; Yoshida et al., 2017; Himeatsu & Furuya, 2016). The rupture process of the $M_w7.1$ Kumamoto earthquake started on the Hinagu fault as a strike-slip event. The rupture crossed the intersection of the Hinagu and Futagawa faults and jumped to the second larger segment. Then, the rupture propagated upward and to NE along the Futagawa fault as a strike-slip with a normal faulting component. Statistics from the ensemble of all models then show that the above features are well constrained by the data. This feature is thus consistently retrieved by other researchers using other methods. The same phenomenon also exists in big data analysis, where even a simple analysis can provide satisfactory results if there is a huge data volume. Contrary to it, the ensemble statistics reveals that the deep zone of a larger slip on the Hinagu fault and the shallow slip zone on the NE part of Futagawa fault are uncertain. The latter is in agreement with the fact that these features are not consistently imaged in the other published slip models.

Appendix A: Biharmonic Spline Interpolation

Two-dimensional biharmonic spline interpolation (Sandwell, 1987) is used for minimum curvature smooth interpolation of a surface from finite number N_c of irregularly spaced control (spline) points. Each spline point c has assigned value A_c (i.e., amplitude) and position specified by coordinates (x_c, y_c) . The interpolating surface is then the result of a linear combination of biharmonic functions $|z|^2(\ln|z|-1)$, where $|z|$ has the meaning of two-dimensional distance between interpolated and spline points.

In particular, the i th interpolated value A_i at given position (x_i, y_i) is given by

$$A_i(x_i, y_i) = \sum_{c=1}^{N_c} \epsilon_c |z|^2 (\ln|z|-1), \quad (A1)$$

where distance $|z|$ is

$$|z| = \sqrt{(x_i - x_c)^2 + (y_i - y_c)^2}. \quad (A2)$$

The “strength” (i.e., weight) of each spline point $\epsilon_c = \epsilon_{c'}$ is found by solving the following linear system of N_c equations:

$$A_c(x_c, y_c) = \sum_{c'=1}^{N_c} \epsilon_{c'} |z'|^2 (\ln|z'|-1), \text{ where } c = 1 \dots N_c, \quad (A3)$$

and $|z'|$ are interspline two-dimensional distances

$$|z'| = \sqrt{(x_c - x_{c'})^2 + (y_c - y_{c'})^2}. \quad (A4)$$

As the system in equation (A3) is linear, the values of $\epsilon_{c'}$ can be calculated prior to the interpolation.

In our particular application to the spatial parametrization of the slip function, we allow amplitude A_c at each spline control point c to vary arbitrarily. Subsequently, the interpolated amplitudes A_i lower than zero are annulled as negative values of the slip are not allowed. Such an approach permits us to generate even sharp interpolated distributions with varying spatial complexity.

Appendix B: Approximate Covariance Function

The covariance matrix of GFs can be estimated by the approach of Hallo and Gallovič (2016). They compose covariance matrices from discrete-time samples of approximate covariance functions $f_n^{\text{ACF}}(t, \varphi)$ depending on time t and time lag φ , reading

$$f_n^{\text{ACF}}(t, \varphi) = \frac{1}{L} \int_{-\frac{L}{2}}^{\frac{L}{2}} u_n(t-l) u_n(t+\varphi-l) dl - \frac{1}{L} \int_{-\frac{L}{2}}^{\frac{L}{2}} u_n(t-l) dl \frac{1}{L} \int_{-\frac{L}{2}}^{\frac{L}{2}} u_n(t+\varphi-l) dl. \quad (\text{B1})$$

Here $u_n(t)$ is the n th component of observed waveforms and $0.5L$ (s) is maximal possible relative time shift of synthetics and observed waveforms caused by imprecise GFs. These time shifts L , as a function of source-receiver distance, can be estimated from time delays caused by randomly perturbed velocity models. Equation (B1) is easy to implement as the integrals normalized by L^{-1} operate as smoothing by a moving time window of width L . For details, see Hallo and Gallovič (2016).

Appendix C: Random Walk With an Efficiently Homogeneous Prior PDF

Implicit or explicit prior assumptions on a model parameter b are present in all inverse problems in general. These priors can be informative (e.g., Gaussian distribution centered at the expected value), weakly informative (e.g., homogeneous in a broad range of values), or noninformative (e.g., homogeneous in \mathbb{R}). In our particular application, we suppress prior assumptions on model parameters by using “efficiently” homogeneous prior PDFs (see equation (22)) within intervals of physically plausible values $B = [b_{\min}, b_{\max}]$, where $b \in B$. This is so not to prefer a priori any particular value between b_{\min} and b_{\max} (i.e., the weakly informative prior) but to have a proper prior (i.e., to avoid the infinitesimal probability).

Such prior PDF is achieved by a random exploration of the model space utilizing Gaussian (i.e., symmetric) proposal distribution q as follows:

$$q(b'|b) = \frac{1}{\sigma\sqrt{2\pi}} \exp\left(-\frac{1}{2}\left(\frac{b'-b}{\sigma}\right)^2\right), \quad (\text{C1})$$

where b' is the new proposed value and σ is the standard deviation of the size of the proposed steps $b \rightarrow b'$. Then, attention has to be paid to the random sampling procedure to preserve homogenous PDF on the random walker occurrence within the whole interval B . The straightforward way is to reject all models having a proposed value b' outside its interval B (i.e., reject the model if $b' \notin B$); however, it results in smaller efficiency of the random walker close to the interval edges (due to higher rejection rate). Hence, we took advantage of the symmetry of the Gaussian distribution, and we utilize the first-order “mirroring” of the proposal distribution on boundaries b_{\min} and b_{\max} as follows:

$$b'' = \begin{cases} 2b_{\min} - b' & \text{if } b' < b_{\min}, \\ 2b_{\max} - b' & \text{if } b' > b_{\max}, \\ b' & \text{if } b' \in B. \end{cases} \quad (\text{C2})$$

We neglect higher orders of repetitive mirroring (i.e., reject the model if $b'' \notin B$) as the size of perturbation $|b' - b|$ in terms of σ is considered small with respect to B . Then, a chain of a large number of steps produce uniformly distributed random samples drawn from B (i.e., efficiently homogeneous prior PDF; see Supporting Information – Figures S1b and S1c), and it is equally efficient within the whole range of B .

List of Abbreviations

ACF	approximate covariance function
CPU	central processing unit
GF	Green's function
JMA	Japan Meteorological Agency
JST	Japan Standard Time
MAP	maximum a posteriori
MC	Monte Carlo
MCMC	Markov chain Monte Carlo
MPI	Message Passing Interface
NASA	National Aeronautics and Space Administration

Acknowledgments

The authors thank all operators involved in station maintenance of K-NET, KiK-net, and F-net networks (National Research Institute for Earth Science and Disaster Resilience [NIED], 2019a, 2019b). We also thank all people involved in the SIV project, and administration and research workers from our institutions (Swiss Seismological Service, SED, ETH Zurich; and Department of Geophysics, Charles University). Special thanks go to Prof. Malcolm Cambridge for our discussion about transdimensional proposal distributions. We are grateful to two anonymous reviewers for their comments that improved the original manuscript. This study makes use of the computer package Parallel Tempering, which was made available with support from the Inversion Laboratory (ilab). ilab is a program for construction and distribution of data inference software in the geosciences supported by AuScope Ltd, a nonprofit organization for Earth Science infrastructure, funded by the Australian Federal Government. Next, this study makes use of the packages of the eikonal solver (Podvin & Lecomte, 1991); approximate covariance matrices (Hallos & Gallovič, 2016); and some subroutines from linear multiteme window earthquake slip inversion (Gallovič et al., 2015). The Inkscape GPL software was used to annotate vector images. Generic Mapping Tools (Wessel & Smith, 1998) was used to draw the maps. The topography in maps originates from the SRTM-90m digital elevation data produced originally by NASA, which is hosted by the Consortium for Spatial Information of the Consultative Group for International Agricultural Research at website <http://srtm.csi.cgiar.org>. The calculations were carried out on Salomon supercomputer (Ostrava, Czech Republic), supported by the Ministry of Education, Youth and Sports from the Large Infrastructures for Research, Experimental Development and Innovations project “IT4Innovations National Supercomputing Center—LM2015070” (IT4I supercomputer). Most of this study was carried out at the Department of Geophysics, Charles University. We acknowledge financial support through the bilateral project of the Czech Science Foundation (18-06716J) and DFG (GA 2465/2-1). The project was partly supported by the Swiss Federal Nuclear Safety Inspectorate (ENSI). The waveform data that support the findings of this study are available at the NIED strong-motion website (<http://www.kyoshin.bosai.go.jp>), NIED F-net website (<http://www.fnet.bosai.go.jp>), and

NIED	National Research Institute for Earth Science and Disaster Resilience
PDF	probability density function
PSI	Parametric Slip Inversion
PT	parallel tempering
RAM	random-access memory
RPH	ring polar histogram
SACF	stationarized approximate covariance function
SIV	Source Inversion Validation
SRF	slip rate function
SRTM	Shuttle Radar Topography Mission
trans-D	transdimensional

References

- Akaike, H. (1980). Likelihood and the Bayes procedure. *Trabajos de Estadística Y de Investigación Operativa*, 31(1), 143–166. <https://doi.org/10.1007/BF02888350>
- Aki, K., & Richards, P. G. (2002). *Quantitative seismology* (2nd ed.). Sausalito: University Science Books.
- Aoi, S., Kunugi, T., Nakamura, H., & Fujiwara, H. (2011). Deployment of new strong motion seismographs of K-NET and KiK-net. In S. Akkar, P. Gülkán, & T. van Eck (Eds.), *Earthquake data in engineering seismology geotechnical, geological, and earthquake engineering* (Vol. 14, pp. 167–186). Dordrecht: Springer. https://doi.org/10.1007/978-94-007-0152-6_12
- Archuleta, R. J. (1984). A faulting model for the 1979 Imperial Valley earthquake. *Journal of Geophysical Research*, 89, 4559–4585.
- Asano, K., & Iwata, T. (2009). Source rupture process of the 2004 Chuetsu, Mid-Niigata prefecture, Japan, earthquake inferred from waveform inversion with dense strong-motion data. *Bulletin of the Seismological Society of America*, 99(1), 123–140.
- Asano, K., & Iwata, T. (2016). Source rupture processes of the foreshock and mainshock in the 2016 Kumamoto earthquake sequence estimated from the kinematic waveform inversion of strong data. *Earth, Planets and Space*, 68(147), 1–11.
- Asano, K., Iwata, T., & Irikura, K. (2005). Estimation of source rupture process and strong ground motion simulation of the 2002 Denali, Alaska, earthquake. *Bulletin of the Seismological Society of America*, 95(5), 1701–1715.
- Beresnev, I. A. (2003). Uncertainties in finite-fault slip inversions: To what extent to believe? (A critical review). *Bulletin of the Seismological Society of America*, 93(6), 2445–2458.
- Bishop, C. M. (2006). *Pattern recognition and machine learning*. New York: Springer.
- Bizzarri, A. (2012). Analytical representation of the fault slip velocity from spontaneous dynamic earthquake models. *Journal of Geophysical Research*, 117, B06309.
- Bodin, T., & Sambridge, M. (2009). Seismic tomography with the reversible jump algorithm. *Geophysical Journal International*, 178(3), 1411–1436.
- Bodin, T., Sambridge, M., Tkalcic, H., Arroucau, P., Gallagher, K., & Rawlinson, N. (2012). Transdimensional inversion of receiver functions and surface wave dispersion. *Journal of Geophysical Research*, 117, B02301.
- Bouchon, M. (1981). A simple method to calculate Green's functions for elastic layered media. *Bulletin of the Seismological Society of America*, 71, 959–971.
- Bouchon, M., Toksoz, M. N., Karabulut, H., Bouin, M., Dietrich, M., Aktar, M., & Edie, M. (2002). Space and time evolution of rupture and faulting during the 1999 Izmit (Turkey) earthquake. *Bulletin of the Seismological Society of America*, 92(1), 256–266.
- Causse, M., Cultrera, G., Moreau, L., Herrero, A., Schiappapietra, E., & Courboulex, F. (2017). Bayesian rupture imaging in a complex medium: The 29 May 2012 Emilia, Northern Italy, earthquake. *Geophysical Research Letters*, 44(15), 7783–7792.
- Clévédé, E., Bouin, M. P., Bukchin, B., Mostinskij, A., & Patau, G. (2004). New constraints on the rupture process of the 1999 August 17 Izmit earthquake deduced from estimates of stress glut rate moments. *Geophysical Journal International*, 159(3), 931–942.
- Custodio, S., & Archuleta, R. J. (2007). Parkfield earthquakes: Characteristic or complementary? *Journal of Geophysical Research*, 112, B05310.
- Dettmer, J., Benavente, R., Cummins, P. R., & Sambridge, M. (2014). Trans-dimensional finite-fault inversion. *Geophysical Journal International*, 199, 735–751.
- Dettmer, J., Dosso, S. E., & Holland, C. W. (2007). Uncertainty estimation in seismo-acoustic reflection travel-time inversion. *The Journal of the Acoustical Society of America*, 122(1), 161–176. <https://doi.org/10.1121/1.2736514>
- Dettmer, J., Dosso, S. E., & Holland, C. W. (2010). Trans-dimensional geoaoustic inversion. *The Journal of the Acoustical Society of America*, 128(6), 3393–3405. <https://doi.org/10.1121/1.3500674>
- Duputel, Z., Agram, P. S., Simons, M., Minson, S. E., & Beck, J. L. (2014). Accounting for prediction uncertainty when inferring subsurface fault slip. *Geophysical Journal International*, 197(1), 464–482.
- Duputel, Z., Jiang, J., Jolivet, R., Simons, M., Rivera, L., Ampuero, J.-P., et al. (2015). The Iquique earthquake sequence of April 2014: Bayesian modeling accounting for prediction uncertainty. *Geophysical Research Letters*, 42, 7949–7957. <https://doi.org/10.1002/2015GL065402>
- Fan, Y., & Sisson, S. A. (2011). Reversible jump Markov chain Monte Carlo. In S. Brooks, A. Gelman, G. L. Jones, & X. Meng (Eds.), *Handbook of Markov Chain Monte Carlo* (pp 67–92). Boca Raton: Chapman & Hall/CRC.
- Fukahata, Y., & Hashimoto, M. (2016). Simultaneous estimation of the dip angles and slip distribution on the faults of the 2016 Kumamoto earthquake through a weak nonlinear inversion of InSAR data. *Earth, Planets and Space*, 68(204), 1–10.
- Gallagher, K., Charvin, K., Nielsen, S., Sambridge, M., & Stephenson, J. (2009). Markov chain Monte Carlo (McMC) sampling methods to determine optimal models, model resolution and model choice for earth science problems. *Marine and Petroleum Geology*, 26, 525–535.
- Gallovič, F., & Ampuero, J.-P. (2015). A new strategy to compare inverted rupture models exploiting the eigen-structure of the inverse problem. *Seismological Research Letters*, 86, 1679–1689.

- on the SIV project website (<http://eqquake-rc.info/SIV/>). The authors declare that they have no competing interests.
- Gallović, F., Imperatori, W., & Mai, P. M. (2015). Effects of three-dimensional crustal structure and smoothing constraint on earthquake slip inversions: Case study of the M_w 6.3 2009 L'Aquila earthquake. *Journal of Geophysical Research*, 120, 428–449.
- Gallović, F., Valentová, L., Ampuero, J.-P., & Gabriel, A.-A. (2019a). Bayesian dynamic finite-fault inversion: 1. Method and synthetic test. *Journal of Geophysical Research - Solid Earth*, 124, 6949–6969.
- Gallović, F., Valentová, L., Ampuero, J.-P., & Gabriel, A.-A. (2019b). Bayesian dynamic finite-fault inversion: 2. Application to the 2016 M_w 6.2 Amatrice, Italy, Earthquake. *Journal of Geophysical Research - Solid Earth*, 124, 6970–6988.
- Gallović, F., & Zahradník, J. (2010). Toward understanding slip inversion uncertainty and artifacts: 2. Singular value analysis. *Journal of Geophysical Research*, 116, B02309.
- Geyer, C., & Moller, J. (1994). Simulation procedures and likelihood inference for spatial point processes. *Scandinavian Journal of Statistics*, 21(4), 359–373.
- Green, P. J. (1995). Reversible jump Markov chain Monte Carlo computation and Bayesian model determination. *Biometrika*, 82(4), 711–732.
- Green, P. J. (2003). Trans-dimensional Markov chain Monte Carlo. In P. J. Green, N. L. Hjorf & S. Richardson (Eds.), *Highly structured stochastic systems* (pp 179–198). Oxford: Oxford University Press.
- Hallo, M., Asano, K., & Gallović, F. (2017). Bayesian inference and interpretation of centroid moment tensors of the 2016 Kumamoto earthquake sequence, Kyushu, Japan. *Earth, Planets and Space*, 69(134), 1–19.
- Hallo, M., & Gallović, F. (2016). Fast and cheap approximation of Green functions uncertainty for waveform-based earthquake source inversions. *Geophysical Journal International*, 207(2), 1012–1029.
- Hao, J., Ji, C., & Yao, Z. (2017). Slip history of the 2016 M_w 7.0 Kumamoto earthquake: Intraplate rupture in complex environment. *Geophysical Research Letters*, 44, 743–750.
- Hartzell, S., Liu, P., Mendoza, C., Ji, C., & Larson, K. M. (2007). Stability and uncertainty of finite-fault slip inversions: Application to the 2004 Parkfield, California, earthquake. *Bulletin of the Seismological Society of America*, 97(6), 1911–1934.
- Hartzell, S. H., & Heaton, T. H. (1983). Inversion of strong ground motion and teleseismic waveform data for the fault rupture history of the 1979 Imperial Valley, California earthquake. *Bulletin of the Seismological Society of America*, 73(6), 1553–1583.
- Hastings, W. K. (1970). Monte Carlo sampling methods using Markov Chains and their applications. *Biometrika*, 57, 97–109.
- Hawkins, R., Bodin, T., Sambridge, M., Choblet, G., & Husson, L. (2019). Trans-dimensional surface reconstruction with different classes of parameterization. *Geochemistry, Geophysics, Geosystems*, 20, 505–529.
- Hawkins, R., & Sambridge, M. (2015). Geophysical imaging using trans-dimensional trees. *Geophysical Journal International*, 203, 972–1000. <https://doi.org/10.1093/gji/ggv326>
- Himematsu, Y., & Furuya, M. (2016). Fault source model for the 2016 Kumamoto earthquake sequence based on ALOS-2/PALSAR-2 pixel-offset data: Evidence for dynamic slip partitioning. *Earth, Planets and Space*, 68(169), 1–10.
- Ide, S. (2007). Slip inversion. In H. Kanamori (Ed.), *Treatise on geophysics* (Vol. 4, pp 193–223). Amsterdam: Elsevier.
- Ji, C., Wald, D. J., & Helmberger, D. V. (2002). Source description of the 1999 Hector Mine, California, earthquake, Part I: Wavelet domain inversion theory and resolution analysis. *Bulletin of the Seismological Society of America*, 92(4), 1192–1207.
- Kato, A., Fukuda, J., Nakagawa, S., & Kazushige, O. (2016). Foreshock migration preceding the 2016 M_w 7.0 Kumamoto earthquake, Japan. *Geophysical Research Letters*, 43(17), 8945–8953.
- Kirkpatrick, S., Gelatt, C. D. J., & Vecchi, M. P. (1983). Optimization by simulated annealing. *Science*, 220, 671–680.
- Kobayashi, H., Koketsu, K., & Miyake, H. (2017). Rupture processes of the 2016 Kumamoto earthquake sequence: Causes for extreme ground motions. *Geophysical Research Letters*, 44(12), 6002–6010.
- Koketsu, K., Miyake, H., & Suzuki, H. (2012). Japan integrated velocity structure model version 1., In: Proceedings of the 15th World Conference on Earthquake Engineering, Lisbon, 24–28 Sept 2012.
- Kubo, H., Asano, K., Iwata, T., & Aoi, S. (2016). Development of fully Bayesian multiple-time-window source inversion. *Geophysical Journal International*, 204(3), 1601–1619. <https://doi.org/10.1093/gji/ggv540>
- Kubo, H., Suzuki, W., Aoi, S., & Sekiguchi, H. (2016). Source rupture processes of the 2016 Kumamoto, Japan, earthquakes estimated from strong-motion waveforms. *Earth, Planets and Space*, 68(161), 1–13.
- Liu, P., & Archuleta, R. J. (2004). A new nonlinear finite fault inversion with three-dimensional Green's functions: Application to the 1989 Loma Prieta, California, earthquake. *Journal of Geophysical Research*, 109, B02318.
- Mai, P. M., Schorlemmer, D., Page, M., Ampuero, J., Asano, K., Causse, M., et al. (2016). The earthquake-Source Inversion Validation (SIV) project. *Seismological Research Letters*, 87(3), 690–708.
- Metropolis, N., Rosenbluth, A., Rosenbluth, M., Teller, A., & Teller, E. (1953). Equation of state calculations by fast computing machines. *The Journal of Chemical Physics*, 21, 1081–1092.
- Minson, S. E., Simons, M., & Beck, J. L. (2013). Bayesian inversion for finite fault earthquake source models. I—Theory and algorithm. *Geophysical Journal International*, 194(3), 1701–1726. <https://doi.org/10.1093/gji/ggt180>
- Minson, S. E., Simons, M., Beck, J. L., Ortega, F., Jiang, J., Owen, S. E., et al. (2014). Bayesian inversion for finite fault earthquake source models—I: The 2011 great Tohoku-oki, Japan earthquake. *Geophysical Journal International*, 198, 922–940.
- Monelli, D., Mai, P. M., Jónsson, S., & Giardini, D. (2009). Bayesian imaging of the 2000 Western Tottori (Japan) earthquake through fitting of strong motion and GPS data. *Geophysical Journal International*, 176(1), 135–150.
- Nakata, T., & Imaizumi, T. (2002). *Digital active fault map of Japan*. Tokyo: University of Tokyo Press. (in Japanese)
- National Research Institute for Earth Science and Disaster Resilience (2019a). NIED K-NET, KiK-net, National Research Institute for Earth Science and Disaster Resilience, doi:10.17598/NIED.0004.
- National Research Institute for Earth Science and Disaster Resilience (2019b). NIED F-net, National Research Institute for Earth Science and Disaster Resilience, doi:10.17598/NIED.0005.
- Okada, Y., Kasahara, K., Hori, S., Obara, K., Sekiguchi, S., Fujiwara, H., & Yamamoto, A. (2004). Recent progress of seismic observation networks in Japan—Hi-net, F-net, K-NET and KiK-net. *Earth, Planets and Space*, 56, xv–xxviii.
- Olson, A. H., & Apsel, R. J. (1982). Finite faults and inverse theory with applications to the 1979 Imperial Valley earthquake. *Bulletin of the Seismological Society of America*, 72(6A), 1969–2001.
- Piatanesi, A., Cirella, A., Spudich, P., & Cocco, M. (2007). A global search inversion for earthquake kinematic rupture history: Application to the 2000 western Tottori, Japan earthquake. *Journal of Geophysical Research*, 112(B7), B07314. <https://doi.org/10.1029/2006JB004821>
- Pizzi, A., Di Domenica, A., Gallović, F., Luzi, L., & Puglia, R. (2017). Fault segmentation as constraint to the occurrence of the main shocks of the 2016 Central Italy seismic sequence. *Tectonics*, 36, 2370–2387.
- Podvin, P., & Lecomte, I. (1991). Finite difference computation of traveltimes in very contrasted velocity models: A massively parallel approach and its associated tools. *Geophysical Journal International*, 105(1), 271–284.

- Ragon, T., Sladen, A., & Simons, M. (2018). Accounting for uncertain fault geometry in earthquake source inversions—I: Theory and simplified application. *Geophysical Journal International*, 214, 1174–1190.
- Ragon, T., Sladen, A., & Simons, M. (2019). Accounting for uncertain fault geometry in earthquake source inversions—II: Application to the M_w 6.2 Amatrice earthquake, central Italy. *Geophysical Journal International*, 218, 689–707.
- Sambridge, M. (2014). A parallel tempering algorithm for probabilistic sampling and multimodal optimization. *Geophysical Journal International*, 196(1), 357–374.
- Sambridge, M., Gallagher, K., Jackson, A., & Rickwood, P. (2006). Transdimensional inverse problems, model comparison and the evidence. *Geophysical Journal International*, 167, 528–542.
- Sandwell, D. T. (1987). Biharmonic splines interpolation of GEOS-3 and SEASAT altimeter data. *Geophysical Research Letters*, 14(2), 139–142.
- Sekiguchi, H., Irikura, K., & Iwata, T. (2000). Fault geometry in the rupture termination of the 1995 Hyogo-ken Nanbu earthquake. *Bulletin of the Seismological Society of America*, 90(1), 117–133.
- Sekiguchi, H., & Iwata, T. (2002). Rupture process of the 1999 Kocaeli, Turkey, earthquake estimated from strong-motion waveforms. *Bulletin of the Seismological Society of America*, 92(1), 300–311.
- Shimizu, K., Yagi, Y., Okuwaki, R., & Fukahata, Y. (2020). Development of an inversion method to extract information on fault geometry from teleseismic data. *Geophysical Journal International*, 220(2), 1055–1065.
- Spudich, P., Cirella, A., Scognamiglio, L., & Tinti, E. (2019). Variability in synthetic earthquake ground motions caused by source variability and errors in wave propagation models. *Geophysical Journal International*, 219(1), 346–372.
- Tarantola, A. (2005). *Inverse problem theory and methods for model parameter estimation*. Philadelphia: Society for Industrial and Applied Mathematics.
- Tarantola, A., & Valette, B. (1982). Inverse problems = quest for information. *Journal of Geophysics*, 50(3), 159–170.
- Tinti, E., Fukuyama, E., Piatanesi, A., & Cocco, M. (2005). A kinematic source-time function compatible with earthquake dynamics. *Bulletin of the Seismological Society of America*, 95(4), 1211–1223.
- Valentová, L., Gallovič, F., & Maierová, P. (2017). Three-dimensional S-wave velocity model of the Bohemian Massif from Bayesian ambient noise tomography. *Tectonophysics*, 717, 484–498.
- Wald, D. J., & Heaton, T. H. (1994). Spatial and temporal distribution of slip for the 1992 Landers, California, earthquake. *Bulletin of the Seismological Society of America*, 84, 668–691.
- Wessel, P., & Smith, W. H. F. (1998). New, improved version of generic mapping tools released. *Eos, Transactions of the American Geophysical Union*, 79, 579.
- Yabuki, T., & Matsu'ura, M. (1992). Geodetic data inversion using a Bayesian information criterion for spatial distribution of fault slip. *Geophysical Journal International*, 109, 363–375.
- Yagi, Y., & Fukahata, Y. (2011). Introduction of uncertainty of Green's function into waveform inversion for seismic source processes. *Geophysical Journal International*, 186(2), 711–720.
- Yoshida, K., Miyakoshi, K., Somei, K., & Irikura, K. (2017). Source process of the 2016 Kumamoto earthquake (M_j 7.3) inferred from kinematic inversion of strong-motion records. *Earth, Planets and Space*, 69(64), 1–13.
- Záhradník, J., & Gallovič, F. (2010). Toward understanding slip-inversion uncertainty and artifacts. *Journal of Geophysical Research*, 115, B09310.